

Article

Enhanced Degradation of Rhodamine B through Peroxymonosulfate Activated by a Metal Oxide/Carbon Nitride Composite

Yuanmin Mo ^{1,2}, Wei Xu ^{1,2}, Xiaoping Zhang ^{1,2,3,4,*} and Shaoqi Zhou ^{1,2,3}

- ¹ School of Environment & Energy, South China University of Technology, Guangzhou Higher Education Mega Centre, Guangzhou 510006, China; yuanminmo@163.com (Y.M.); xuwei06042022@163.com (W.X.); fesqzhou@yeah.net (S.Z.)
- ² The Key Laboratory of Pollution Control and Ecosystem Restoration in Industry Clusters of Ministry of Education, Guangzhou 510006, China
- ³ Guangdong Provincial Key Laboratory of Solid Wastes Pollution Control and Recycling, Guangzhou 510006, China
- ⁴ Guangdong Provincial Engineering and Technology Research Center for Environmental Risk Prevention and Emergency Disposal, Guangzhou 510006, China
- * Correspondence: xpzhang@scut.edu.cn; Tel.: +86-13678920429

Abstract: The development of high catalytic performance heterogeneous catalysts such as peroxy-monosulfate (PMS) activators is important for the practical remediation of organic pollution caused by Rhodamine B (RhB). An economical and facile synthesized composite of copper–magnesium oxide and carbon nitride (CM/g-C₃N₄) was prepared by the sol-gel/high-temperature pyrolysis method to activate PMS for RhB degradation. CM/g-C₃N₄ exhibited a splendid structure for PMS activation, and the aggregation of copper–magnesium oxide was decreased when it was combined with carbon nitride. The introduction of magnesium oxide and carbon nitride increased the specific surface area and pore volume of CM/g-C₃N₄, providing more reaction sites. The low usage of CM/g-C₃N₄ (0.3 g/L) and PMS (1.0 mM) could rapidly degrade 99.88% of 10 mg/L RhB, and the RhB removal efficiency maintained 99.30% after five cycles, showing the superior catalytic performance and reusability of CM/g-C₃N₄. The synergistic effect of copper and g-C₃N₄ improved the PMS activation. According to the analyses of EPR and quenching experiments, SO₄^{•−}, •OH and O₂^{•−} radicals and ¹O₂ were generated in the activation of PMS, of which SO₄^{•−} and ¹O₂ were important for RhB removal. The toxicity of RhB was alleviated after being degraded by the CM/g-C₃N₄/PMS system. This study provides an efficient and promising strategy for removing dyes in water due to the hybrid reaction pathways in the CM/g-C₃N₄/PMS system.

Keywords: RhB degradation; heterogeneous catalyst; copper–magnesium oxide/carbon nitride composite; PMS activation



Citation: Mo, Y.; Xu, W.; Zhang, X.; Zhou, S. Enhanced Degradation of Rhodamine B through Peroxymonosulfate Activated by a Metal Oxide/Carbon Nitride Composite. *Water* **2022**, *14*, 2054. <https://doi.org/10.3390/w14132054>

Academic Editors: Dionysios (Dion) Demetriou Dionysiou, Yujue Wang and Huijiao Wang

Received: 17 June 2022

Accepted: 25 June 2022

Published: 27 June 2022

Publisher's Note: MDPI stays neutral with regard to jurisdictional claims in published maps and institutional affiliations.



Copyright: © 2022 by the authors. Licensee MDPI, Basel, Switzerland. This article is an open access article distributed under the terms and conditions of the Creative Commons Attribution (CC BY) license (<https://creativecommons.org/licenses/by/4.0/>).

1. Introduction

Rhodamine B (RhB) poses a potential threat to the aquatic environment and human health because of its high salt content and poor biodegradability [1]. RhB has been extensively applied in the fields of colored glass, as well as the textile and plastic industries. It can cause symptoms such as the red staining of human skin, mild congestion of blood vessels in the brain and breakage of myocardial fibers. According to the chemical carcinogenic risk assessment of the World Health Organization International Agency for Research on Cancer (IARC), ingestion or skin contact with RhB will cause acute and chronic poisoning. Therefore, exploring efficient treatment technology is important for removing the highly toxic RhB.

Many methods have emerged to remove RhB, including adsorption [2], ion exchange [3], advanced oxidation processes (AOPs) [4,5], membrane filtration [6] and biodegradation [7].

However, owing to its special chemical structural stability, light resistance, corrosion resistance and bacteriostasis, RhB cannot be fully degraded by traditional physical methods and biological technologies [4]. Among them, AOPs have garnered extensive attention for their high efficiency and mineralization in removing pollutants [8–10]. Traditional AOPs use hydroxyl radicals ($\bullet\text{OH}$) to remove pollutants [11]. However, the problems of weak redox potential (1.8–2.7 V), short lifetime ($<1\ \mu\text{s}$) and a narrow range of optimum pH restrict the application of $\bullet\text{OH}$ [12]. Recently, AOPs based on sulfate radicals ($\text{SO}_4^{\bullet-}$) have received more and more attention for their high redox potential (2.5–3.1 V), long lifetime (30–40 ms) and a wide pH range [13]. Peroxymonosulfate (PMS) is one of the widely used oxidants activated by transition metal ions [14,15], heat [16], alkali materials [17], ultrasound [18], UV light sources (254 nm) [19] and heterogeneous catalysts [20] to produce $\text{SO}_4^{\bullet-}$ for pollutant degradation. Among various methods, PMS activated by heterogeneous catalysts is more promising for practical applications because of its mild reaction conditions, low energy consumption and easy recycling [20]. Previous research has employed heterogeneous catalysts including CuO [21], CuCo_2O_4 [22], $\text{CuO@FeO}_x\text{/Fe-0}$ [23] and $\text{CuO-Co}_3\text{O}_4\text{@CeO}_2$ [24] to activate PMS for pollutant degradation. All these studies have demonstrated that PMS activated by metal oxide for the generation of active substance is a prospective advanced oxidation process for the decomposition of toxic pollutants.

Copper is one of the transition metals for PMS activation. Copper oxide, as an efficient, economical and low toxic heterogeneous catalyst, has a high catalytic performance [25]. However, the problems with the aggregation and the dissolution of copper ion decrease the activity and limit the practical application of copper oxide. To overcome such drawbacks, Du et al. prepared CuO/rGO for 2,4,6-trichlorophenol removal, which exhibited much better catalytic performance than CuO [26]. Kiain et al. found that CuO@AC could be reused in three cycles, and the leaching of copper ions was negligible [27]. Li et al. synthesized BC-CuO for methylene blue, acid orange 7, atrazine and ciprofloxacin removal in a highly saline system, which achieved a high catalytic performance [28]. All these results indicated that loading the copper oxide on the supporter is an efficient way to improve the catalytic performance of copper oxide. However, the applications of these catalysts were restricted by the complex synthesis, high cost of precursor materials and insufficient reaction sites. Therefore, it is necessary to develop a method of low-cost and facile synthesis and increase the reaction site to enhance the catalytic performance of copper oxide.

Carbon nitride ($\text{g-C}_3\text{N}_4$), as a low-cost and stable material, is commonly applied in many fields [29–31], which could be easily prepared by being calcined in the air, without any chemical or physical pretreatment. The $\text{g-C}_3\text{N}_4$ can not only be used as a supporter to disperse the metal oxide, with more reaction sites exposed, but also activate PMS to some extent. Therefore, the introduction of $\text{g-C}_3\text{N}_4$ may decrease the aggregation and improve the catalytic performance of copper oxide. It is reported that the introduction of magnesium oxide can enhance the specific surface area and electron transfer capacity of the catalyst [32–34], which is beneficial for PMS activation. Furthermore, the large quantities of surface basic sites on magnesium oxide can facilitate the formation of an M–OH complex [34], thus increasing the reaction sites between the catalyst and PMS, which is the vital step for PMS activation. Hence, the combination of copper oxide, magnesium oxide and $\text{g-C}_3\text{N}_4$ is an effective way to improve the catalytic performance of copper oxide. Moreover, it is an economical and eco-friendly catalyst worth exploring.

In order to develop a high catalytic performance catalyst with a low cost and abundant reaction sites for RhB degradation, copper oxide was combined with magnesium oxide and $\text{g-C}_3\text{N}_4$ to form a composite (CM/ $\text{g-C}_3\text{N}_4$). The composite was initially employed as a heterogeneous catalyst for PMS activation, which showed splendid catalytic performance and stability. When compared with previous reports, low-cost magnesium oxide and $\text{g-C}_3\text{N}_4$ were introduced into the catalyst at the same time for increasing the reaction sites and decreasing the aggregation of copper oxide. Furthermore, the hybrid reaction pathways (radicals and non-radical) were produced in the CM/ $\text{g-C}_3\text{N}_4$ /PMS system.

In this study, the effects of preparation procedures on the catalytic performance of composite were investigated, and the effects of catalyst dosage, PMS concentration, RhB concentration and initial pH value on the RhB removal were also explored. The degradation intermediates of RhB were analyzed by LC-MS, and the toxicity was predicted by the Toxicity Estimation Software Tool. The activation mechanism of PMS was proposed according to the results of XPS, the EPR test and quenching experiments. The reusability of the catalyst was conducted through five cycle experiments.

2. Material and Methods

2.1. Chemicals and Reagents

The information relating to the chemicals and reagents is described in supplementary material—Text S1.

2.2. Preparation of Catalyst

A preparation of pure g-C₃N₄: 5 g melamine was placed in a 30 mL quartz crucible and calcined at 550 °C (5 °C/min) for 4 h in an air atmosphere. After cooling down, it was fully ground with an agate mortar to obtain yellow powder.

Preparation of the copper–magnesium oxide/g-C₃N₄ composite (CM/g-C₃N₄): First, 0.250 M Cu(NO₃)₂·3H₂O and 0.250 M Mg(NO₃)₂·6H₂O were dissolved in 40 mL of deionized water. Then, 0.50 M citric acid was added to the above solution and stirred for 10 min. Thereafter, the mixture was heated at 80 °C in the air until the water was completely evaporated to obtain a blue colloid. The obtained colloid was heated to 700 °C at a rate of 5 °C/min under a nitrogen atmosphere for 4 h to obtain black powder. Finally, the black powder and melamine were ground and mixed at a mass ratio of 1:2, and calcined in the air at 550 °C for 4 h (Scheme S1). In order to investigate the effect of the preparation procedures on the catalytic performance of CM/g-C₃N₄, the materials with different g-C₃N₄ precursors (urea and pure g-C₃N₄), mass ratios of copper–magnesium oxide to melamine (1:1, 1:3, 1:4, 1:5), pyrolysis temperatures (500 °C, 600 °C, 800 °C, 900 °C), pyrolysis times (2 h, 3 h, 5 h, 6 h) and molar ratios of copper to magnesium precursor (1:0.25, 1:0.5, 1:1.5, 1:2) were also synthesized according to the preparation processes of CM/g-C₃N₄. The composites prepared with urea or pure g-C₃N₄ as carbon nitride precursors were denoted as CM/g-C₃N₄ (urea) and CM/g-C₃N₄ (2), respectively. The preparations of copper oxide, copper–magnesium oxide, copper oxide/g-C₃N₄ composite and magnesium oxide/g-C₃N₄ composite were the same as the above processes, unless no Mg(NO₃)₂·6H₂O and melamine, melamine Mg(NO₃)₂·6H₂O and Cu(NO₃)₂·3H₂O were added. They were denoted as CuO, CM, C/g-C₃N₄ and M/g-C₃N₄, respectively.

2.3. Degradation Experiment

The information relating to the degradation experiment was described in supplementary material—Text S2. Three groups of parallel samples were carried out in each experiment. All results are displayed as an average value and standard error.

2.4. Characterizations

The information relating to the characterizations is described in supplementary material—Text S3.

2.5. Analytical Methods

RhB concentration was analyzed by a UV-visible spectrophotometer at 554 nm. The total organic carbon (TOC) concentration was calculated by a TOC analyzer (Muti N/C 2100). Active substances were observed by using an electron paramagnetic resonance spectrometer (EPR, Bruker E 500-10/12). The intermediates of RhB degradation were identified using a liquid chromatography–mass spectrometry machine (LC-MS, Agilent 1290II). The ionization mode was chosen as ESI (positive ion mode), and the source temperature was 350 °C. The mixture of 0.10% formic acid and CH₃CN (60:40, v/v) was the mobile phase,

and the flow rate was 0.20 mL/min. The leaching concentrations of copper and magnesium ions were analyzed by an inductively coupled plasma optical emission spectrometer (ICP-OES, Agilent 720ES). As to the calculation and optimization of RhB molecule, the Fukui Function based on DFT calculation was adopted in Materials Studio software (MS). The Fukui function analysis was analyzed by LDA/PWC in Dmol3 of MS, without taking into account the influence of spin in the calculation [32]. The Fukui function representing free radical (f^0) attacks was used to evaluate the reaction sites of active substances on the molecules. The toxicity of RhB and its intermediates was evaluated by the Toxicity Estimation Software Tool (TEST) version 5.1.1 based on quantitative structure–activity relationships (QSAR) methodologies [35].

The RhB degradation kinetics were fit by the pseudo first order model and the apparent rate constant (k) was calculated according to Equation (1).

$$\ln(C_t/C_0) = -kt \quad (1)$$

where C_t is the RhB concentration at a certain reaction time (t) and C_0 is the initial RhB concentration; t is the reaction time; k is the apparent rate constant. The crystallite size of CM/g-C₃N₄ was calculated from XRD data using the Scherrer Equation (2) [36].

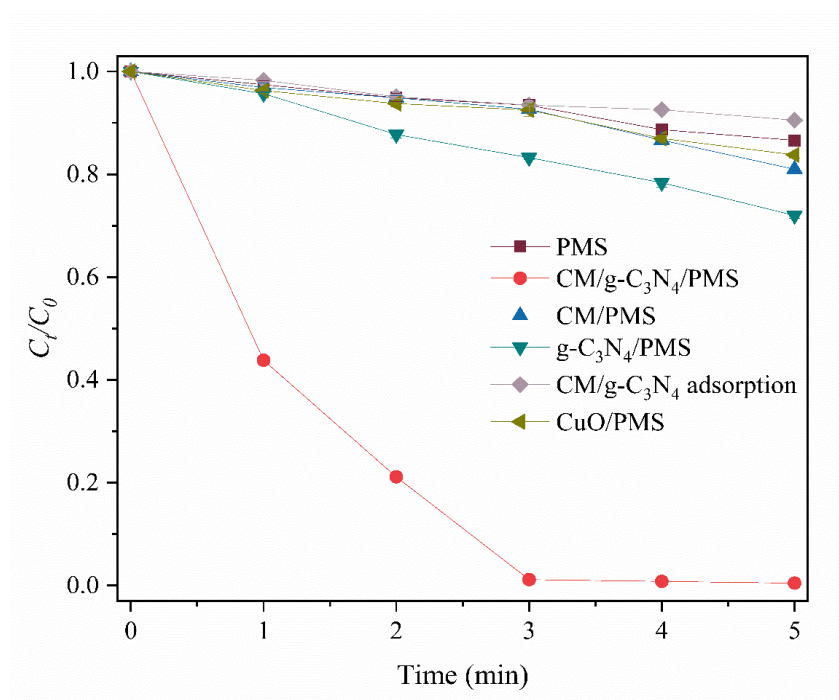
$$D = \frac{K\lambda}{B \cos \theta} \quad (2)$$

where D is the crystallites' size (nm), K is the Scherrer constant (0.9), λ is the wavelength of X-ray sources, B is the FWHM (radians), and θ is the peak position (radians).

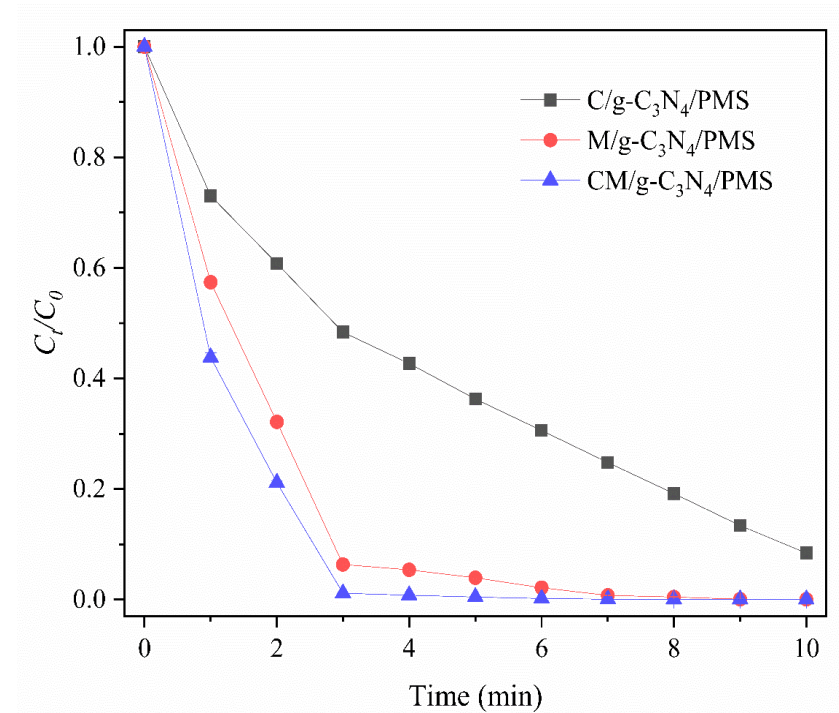
3. Result and Discussion

3.1. Degradation of RhB in Different Systems

As shown in Figure 1a, the removal of RhB by CM/g-C₃N₄ and PMS was 9.47 and 13.42% respectively, indicating that CM/g-C₃N₄ and PMS show poor RhB removal efficiency. Pure g-C₃N₄ could remove 28.01% of RhB in 5 min by activating PMS, demonstrating that g-C₃N₄ is not only a supporter but also can activate PMS to some extent. CM showed a slightly better catalytic performance than CuO, and the catalytic performance of CM was enormously improved when it was combined with g-C₃N₄ to form the CM/g-C₃N₄ composite, with the removal of RhB increasing from 19.03 to 99.53%. Based on the characterizations of SEM and BET, the introduction of g-C₃N₄ could increase the specific surface area and pore volume of CM, and decrease the aggregation of CM, with more reaction sites being exposed. Furthermore, more hydroxyl groups, which were important for PMS activation, were produced on the surface of CM/g-C₃N₄ than that of CM (Sections 3.3.3 and 3.5). Therefore, CM/g-C₃N₄ showed a better catalytic performance than CM. As shown in Figure 1b, the catalytic performances of C/g-C₃N₄ and M/g-C₃N₄ were worse than that of CM/g-C₃N₄. The reason is that the structure of CM/g-C₃N₄ is more conducive for PMS activation than those of C/g-C₃N₄ and M/g-C₃N₄ (Section 3.3). These results indicate that the interaction among copper, magnesium and g-C₃N₄ promotes the catalytic performance of CM/g-C₃N₄. Thus, the CM/g-C₃N₄ is an efficient PMS activator.



(a)



(b)

Figure 1. Degradation of RhB under different systems (a,b). Reaction conditions: [PMS] = 2.0 mM, [catalyst] = 0.50 g/L, [RhB] = 10.0 mg/L, 25 °C.

3.2. Effect of Preparation Procedures on the Catalytic Performance of CM/g-C₃N₄

The effects of preparation conditions, such as g-C₃N₄ formed by different precursors, mass ratios of copper–magnesium oxide to melamine, pyrolysis temperatures and times, and molar ratios of copper to magnesium precursor, on the catalytic performance of CM/g-C₃N₄ were investigated. CM/g-C₃N₄ presented better catalytic performance than CM/g-

C_3N_4 (urea) and showed a similar catalytic performance to CM/g- C_3N_4 (2) (Figure S1a). This is because the decomposition temperature of melamine is higher than that of urea, CM/g- C_3N_4 will form more carbon nitride than CM/g- C_3N_4 (urea) in the preparation process, which is beneficial for PMS activation. Guan et al. (2020) also found that g- C_3N_4 prepared by melamine showed a better catalytic performance than that prepared by urea [37]. To simplify the synthesis process, melamine rather than pure g- C_3N_4 was utilized as the g- C_3N_4 precursor.

As the mass ratio of copper–magnesium oxide to melamine increased from 1:1 to 1:2, the degradation of RhB by CM/g- C_3N_4 /PMS increased in 4 min, while RhB degradation decreased in an increase of the mass ratio from 1:2 to 1:5 (Figure S1b). In a low addition amount, g- C_3N_4 will completely collapse the basic structure [38], and the dispersion of copper–magnesium oxide on the g- C_3N_4 would be inadequate. Furthermore, for a high addition amount of g- C_3N_4 , the dispersion of copper–magnesium oxide was excessive, causing the unsaturated contents of Cu, O and Mg in the CM/g- C_3N_4 . All these phenomena would decrease the catalytic performance of CM/g- C_3N_4 .

The pyrolysis temperature and time have an influence on the catalytic performance of catalysts. When the pyrolysis temperature of CM/g- C_3N_4 was less than 700 °C, the removal of RhB increased with an increase in temperature. However, the removal of RhB decreased as the pyrolysis temperature of CM/g- C_3N_4 reached higher than 700 °C (Figure S1c). It was possible that the structure of the catalyst would be destroyed or collapsed at a much higher pyrolysis temperature [39], thereby reducing reaction sites and decreasing the catalytic performance. The removal of RhB increased in 3 min with CM/g- C_3N_4 heated from 2 to 4 h, while it decreased with CM/g- C_3N_4 heated over 4 h (Figure S1d). This was possible because the structure of the catalyst would be sintered in the long pyrolysis time.

The best molar ratio of copper to magnesium precursors of CM/g- C_3N_4 was explored (Figure S1e). Within 3 min, the removal efficiency of RhB was 48.30, 71.80, 98.93, 73.80 and 66.70% for the molar ratios of copper to magnesium precursor of CM/g- C_3N_4 of 1:0.25, 1:0.5, 1:1, 1:1.5 and 1:2, respectively. The sample was prone to agglomeration and produced other impurities as the molar ratio of copper to magnesium precursor increased or decreased [40]. It could be inferred that the crystal structure of CM/g- C_3N_4 was well constructed in the 1:1 molar ratio of copper to magnesium precursor.

Based on the above results, the catalyst synthesized with a 1:2 mass ratio of copper–magnesium oxide to melamine and a 1:1 molar ratio of copper to magnesium precursor at 700 °C for 4 h, was the best PMS activator.

3.3. Characterizations of the Catalysts

3.3.1. SEM and TEM

For investigating the effect of the microstructure of catalysts on their catalytic performance, SEM characterization was performed, and the distribution of various elements of CM/g- C_3N_4 was also tested by EDS mapping characterization. As shown in Figure 2a,b, CM was composed of particles with aggregation and an irregular shape, and the pure g- C_3N_4 was a sheet packing structure. The aggregation of CM decreased when it was combined with g- C_3N_4 (Figure 2c). The above results showed that CM was well dispersed on the g- C_3N_4 , thus exposing more reaction sites and improving the catalytic performance. The C/g- C_3N_4 were accumulated in a cluster, and no obvious particles had been seen, indicating that the CuO was covered and piled up with the g- C_3N_4 ; thus, fewer reaction sites were exposed (Figure 2e). The structures of CuO and g- C_3N_4 in C/g- C_3N_4 had been changed. On the contrary, M/g- C_3N_4 was accumulated in the form of particles, and no obvious flaky structure had been seen (Figure 2f). The research by Hoai Ta et al. showed a similar phenomenon [41]. Compared with C/g- C_3N_4 and M/g- C_3N_4 , g- C_3N_4 kept its structure in the CM/g- C_3N_4 . These results indicated that the interaction among copper, magnesium and g- C_3N_4 would not make the structure of g- C_3N_4 change. The decreasing aggregation and the structure of CM/g- C_3N_4 was more beneficial for exposing the reaction site to activate PMS than that of C/g- C_3N_4 and M/g- C_3N_4 . Therefore, the catalytic per-

formance of CM/g-C₃N₄ was the best among them. As shown in Figure 2d, the structure of CM/g-C₃N₄ did not change significantly after the reaction, but small cracks appeared in some places of CM/g-C₃N₄. It may be caused by the corrosion of CM/g-C₃N₄ during the PMS activation. The results of SEM-EDS mapping showed that C, N, O, Cu and Mg elements were uniformly distributed on the CM/g-C₃N₄, rather than a random mixture of all substances (Figure 2g).

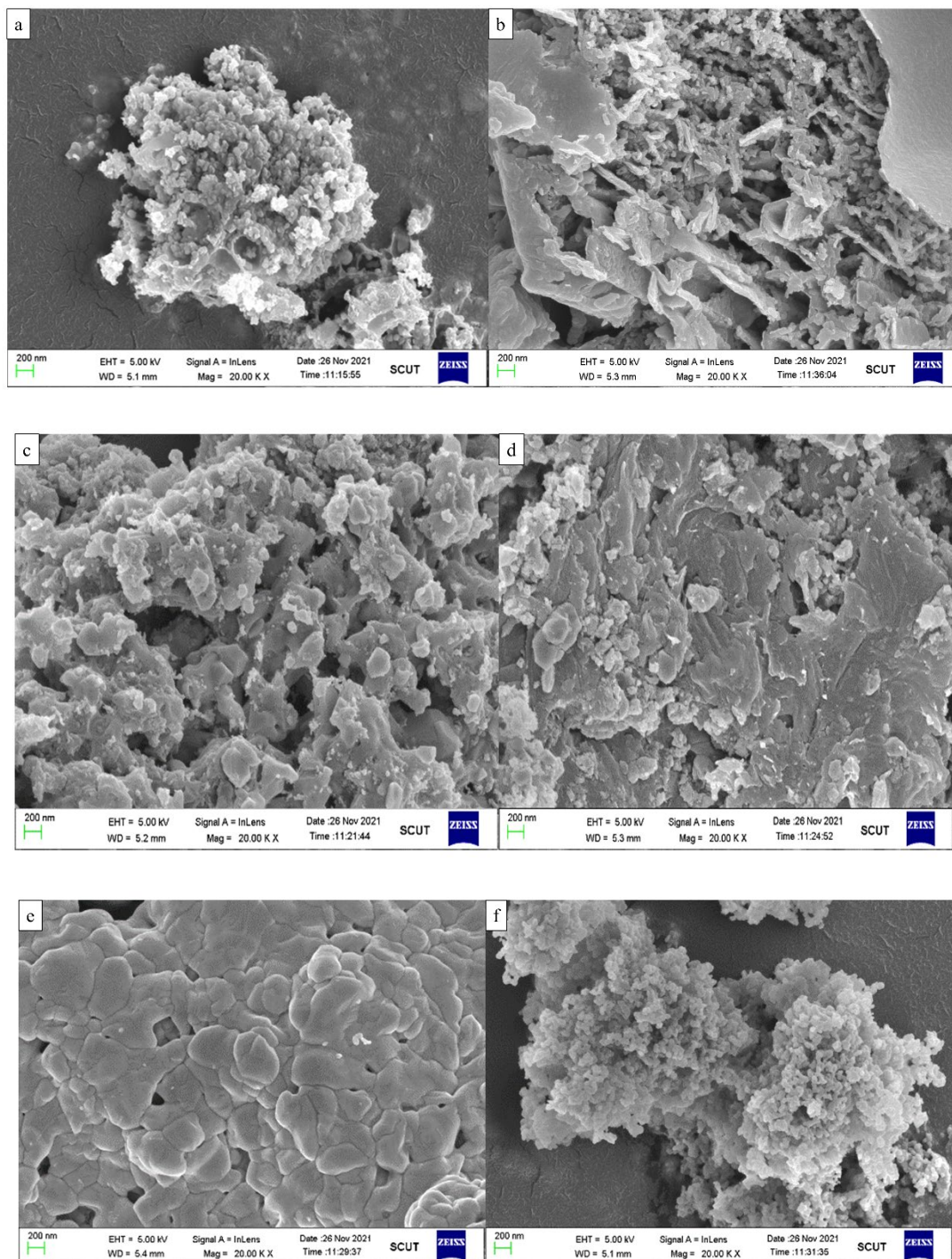


Figure 2. Cont.

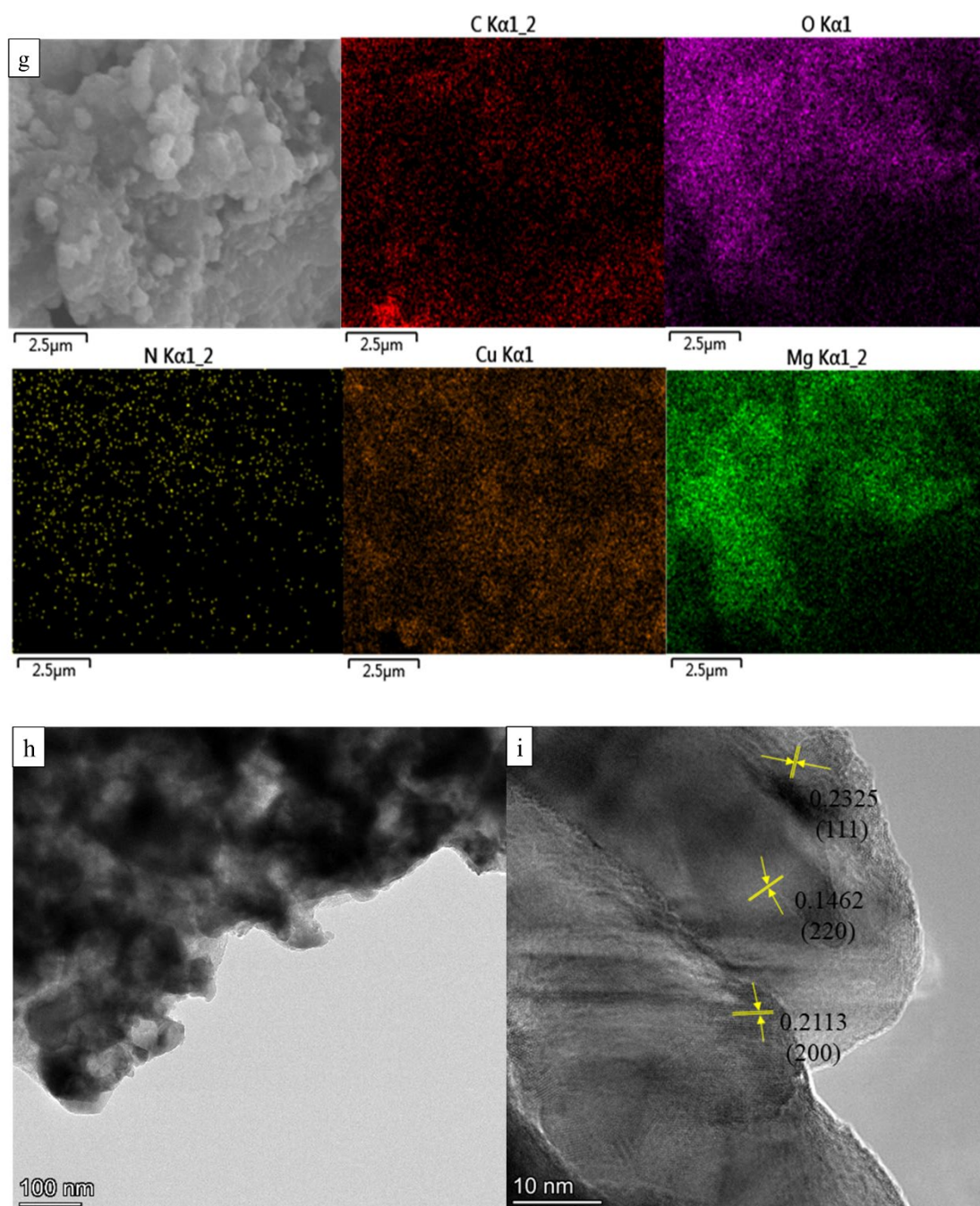


Figure 2. SEM image of CM (a), g-C₃N₄ (b), CM/g-C₃N₄ before (c) and after the reaction (d), C/g-C₃N₄ (e), M/g-C₃N₄ (f), EDS mapping of CM/g-C₃N₄ (g), TEM image (h) and HRTEM image (i) of CM/g-C₃N₄.

Figure 2h clearly shows that the CM was uniformly dispersed on the g-C₃N₄. The HRTEM image of CM/g-C₃N₄ with clear lattice fringes is exhibited in Figure 2i. The lattice spacing was about 0.2325, 0.2113 and 0.1462 nm, corresponding to CuO (111) and MgO (200), (220) crystal planes, respectively. It was consistent with the XRD results (Section 3.3.2).

3.3.2. XRD

The XRD spectra of different catalysts are presented in Figure 3. The peaks at 13.2° and 27.3° in pure g-C₃N₄ were respectively attributed to the in-plane repeating units of the continuous heptazine framework ((100) crystal plane) and the interlayer stacking of

the periodic conjugated aromatic structure ((002) crystal plane) [42–44]. The diffraction peaks of M/g-C₃N₄ at 42.74° and 62.18° corresponded to the (200) and (220) crystal planes of MgO, respectively. The (111) crystal plane attributed to CuO could be observed in the C/g-C₃N₄ at 38.74°. SEM characterization showed that the morphology of g-C₃N₄ in the C/g-C₃N₄ and M/g-C₃N₄ had changed, therefore the g-C₃N₄ diffraction peaks were not found in these two materials. The corresponding peaks of CuO and MgO appeared in the CM, and the aggregation of CM led to the low intensity. The crystal plane diffraction peaks of g-C₃N₄ (002), CuO (111) and MgO (200, 220) were detected at 25.18°, 38.7°, 42.84° and 62.52° of CM/g-C₃N₄, respectively. It was in agreement with the HRTEM result. Due to the irregular arrangement of tri-s-triazine units [45,46], CM/g-C₃N₄ showed a weak (100) crystal plane diffraction peak. The diffraction peak of the (002) crystal plane in CM/g-C₃N₄ was weakened and shifted when compared with pure g-C₃N₄. This phenomenon indicated that the layered g-C₃N₄ was peeled off, and copper–magnesium oxide was successfully introduced into the structure of g-C₃N₄. When compared with pure CuO (JCPDS: 80-1916) and MgO (JCPDS: 79-0612), the corresponding crystal planes in the CM/g-C₃N₄ were slightly shifted, showing that there was an interaction between CuO and MgO in the CM/g-C₃N₄. Furthermore, the XRD peak of CM/g-C₃N₄ was more broadening than that of CM. It could be ascribed to the interaction among copper oxide, magnesium oxide and g-C₃N₄. According to the calculation of the Scherrer equation, the size distribution of CM/g-C₃N₄ was 22.01–63.54 nm, and the average size was 36.94 nm. The XRD spectra of CM/g-C₃N₄ before and after the reaction were similar, but the peak of (002) crystal plane shifted from 25.18° to 26.2° as the intensity decreased. Furthermore, the diffraction peaks of (200) and (220) crystal planes at 42.74° and 62.18° of CM/g-C₃N₄ disappeared after the reaction. The results show that the g-C₃N₄ and MgO in CM/g-C₃N₄ have important effects on the PMS activation.

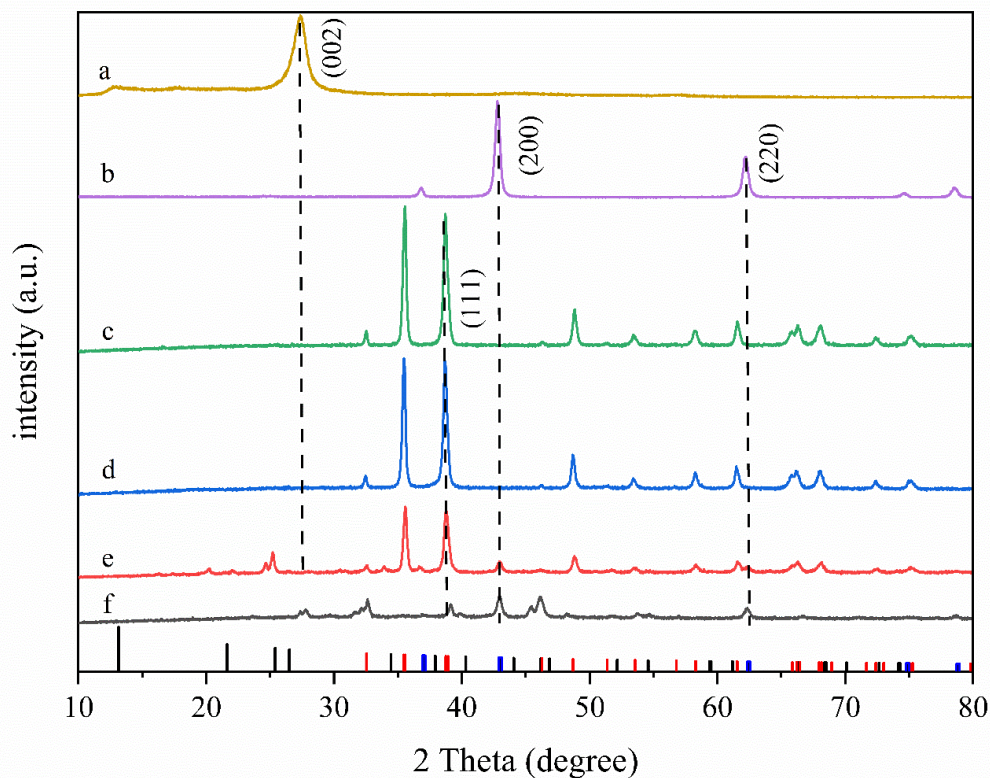


Figure 3. XRD spectra of different catalysts, g-C₃N₄, M/g-C₃N₄, C/g-C₃N₄, used CM/g-C₃N₄, fresh CM/g-C₃N₄ and CM. Black: g-C₃N₄ (JCPDS: 87-1526); Red: CuO (JCPDS: 80-1916); Blue: MgO (JCPDS: 79-0612).

3.3.3. FTIR

The FTIR spectrum of each sample is shown in Figure 4. The peak at 3375 cm^{-1} could be assigned to the stretching vibration of a hydroxyl group ($-\text{OH}$) [47]. This peak was observed in the $\text{M/g-C}_3\text{N}_4$. It could be ascribed to the MgO in $\text{M/g-C}_3\text{N}_4$, which was in favor of $-\text{OH}$ being absorbed on the surface. The peak of $-\text{OH}$ was also observed in the $\text{CM/g-C}_3\text{N}_4$, with a higher intensity than that seen in the $\text{M/g-C}_3\text{N}_4$, but there were no peaks in the CM and $\text{C/g-C}_3\text{N}_4$. The result indicated that the large number of $-\text{OH}$ on the $\text{CM/g-C}_3\text{N}_4$ surface could be attributed to the interaction between MgO and $\text{g-C}_3\text{N}_4$. It may be because the aggregation of CM was not beneficial for $-\text{OH}$ produced on the surface. However, the aggregation was decreased when CM was combined with $\text{g-C}_3\text{N}_4$, and in the action of MgO , $-\text{OH}$ could be produced on the surface of $\text{CM/g-C}_3\text{N}_4$. $-\text{OH}$ has been certified as an important PMS activation site [48], thus the excellent catalytic performance of $\text{CM/g-C}_3\text{N}_4$ can be attributed to the numerous $-\text{OH}$ (demonstrated in Section 3.5). The peak at 1635 cm^{-1} of $\text{CM/g-C}_3\text{N}_4$ could be ascribed to the $-\text{OH}$ bending vibration in adsorbed water [49], which is also important for PMS activation. However, this peak was not observed on the other catalysts. The peaks at $1224\text{--}1647$ and 3175 cm^{-1} of pure $\text{g-C}_3\text{N}_4$ were attributed to the stretching vibration of the heterocyclic ring (C-N=C) and N-H [50–55], respectively. This peak of the heterocyclic ring shifted and became weaker in the $\text{CM/g-C}_3\text{N}_4$ ($1083\text{--}1176\text{ cm}^{-1}$), possibly because of the influence of Cu , Mg and O elements on the structure of the C-N=C . The peak at 810 cm^{-1} was associated with the vibration of the triazine unit, but it was not observed in the $\text{CM/g-C}_3\text{N}_4$ due to its irregular arrangement. These phenomena were in agreement with the XRD result. Due to the shape of the $\text{g-C}_3\text{N}_4$ changing in the $\text{C/g-C}_3\text{N}_4$ and $\text{M/g-C}_3\text{N}_4$, their FTIR spectrums showed no characteristic peak about $\text{g-C}_3\text{N}_4$, which was consistent with the results of SEM and XRD. The peaks below 700 cm^{-1} of $\text{C/g-C}_3\text{N}_4$, $\text{M/g-C}_3\text{N}_4$ and $\text{CM/g-C}_3\text{N}_4$ corresponded to the stretching and bending vibrations of M-O (M : Cu and Mg) [39], respectively.

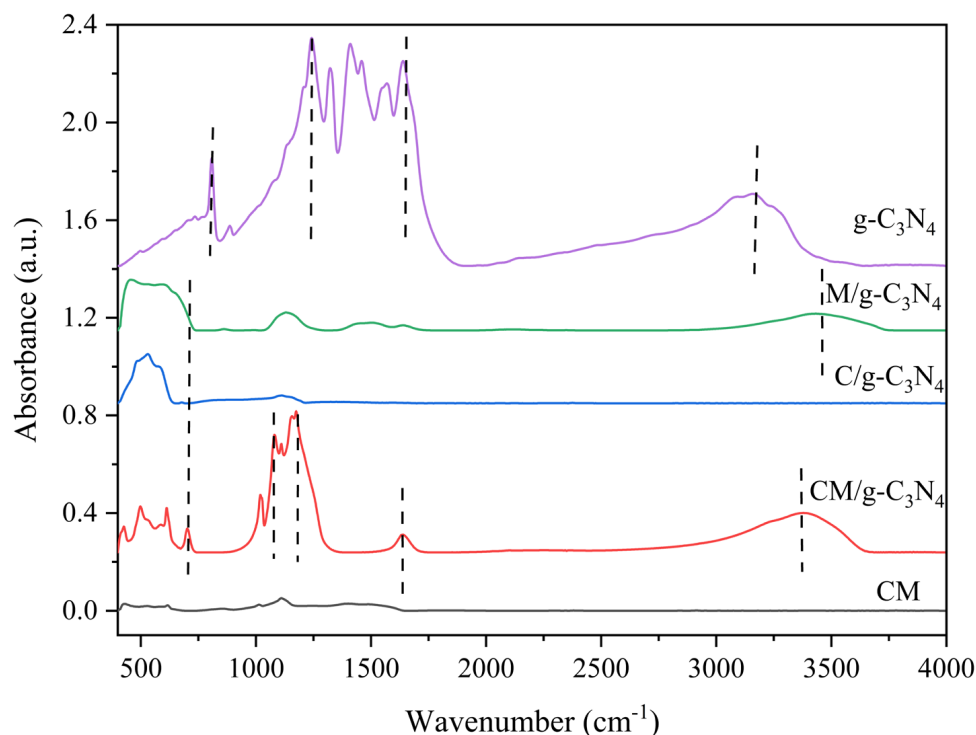


Figure 4. FTIR spectra of different catalysts ($\text{g-C}_3\text{N}_4$; $\text{M/g-C}_3\text{N}_4$; $\text{C/g-C}_3\text{N}_4$; $\text{CM/g-C}_3\text{N}_4$; CM).

3.3.4. BET

A Brunauer-Emmett-Teller (BET) gas adsorption analysis was used to investigate the porous structure and specific surface area (SSA) of the catalyst. All samples showed type

IV isotherms and H₃ type hysteresis loops, indicating that the mesoporous structure was dominant in these samples (Figure 5). When compared with CM and C/g-C₃N₄, the SSA and pore volume of CM/g-C₃N₄ increased, and the average pore diameter slightly reduced (Table 1). These results demonstrated that the introduction of g-C₃N₄ and MgO increased the SSA and pore volume of CM/g-C₃N₄, thus more reaction sites were exposed and the structure of CM/g-C₃N₄ was more conducive to activating PMS. According to the SEM characterizations of CM, C/g-C₃N₄ and CM/g-C₃N₄, the metal oxide in CM/g-C₃N₄ was mostly dispersed. Thus, it could be inferred that the aggregation of the catalyst had a relationship with the SSA. However, the M/g-C₃N₄ with the largest SSA (58.47 m²/g) was accumulated in the form of particles, illustrating that the relationship between SSA and the aggregation of catalyst was not linear. When compared with other materials, such as CuMg-MMO [40] and CuO-CN [45], the SSA, pore volume and average pore diameter of the materials prepared in this article were all the best.

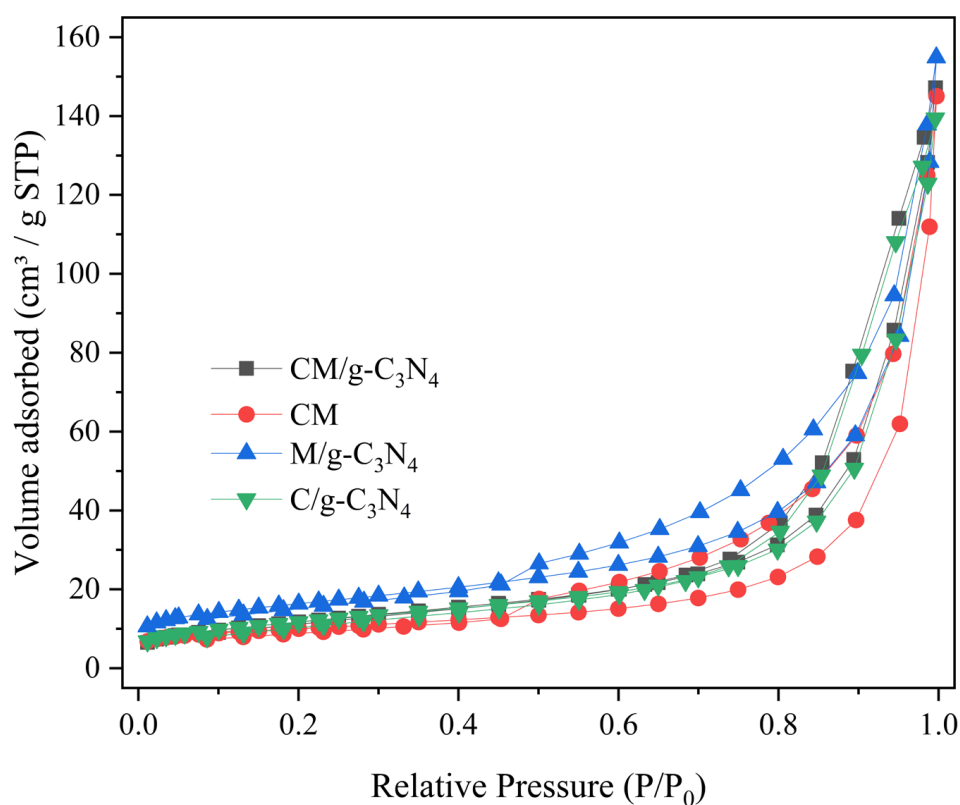


Figure 5. N₂ adsorption–desorption isotherms of different catalysts (g-C₃N₄; M/g-C₃N₄; C/g-C₃N₄; CM/g-C₃N₄; CM).

Table 1. Specific surface area and pore characteristics of different catalysts (g-C₃N₄; M/g-C₃N₄; C/g-C₃N₄; CM/g-C₃N₄; CM).

	Specific Surface Area (m ² /g)	Pore Volume (cm ³ /g)	Pore Size (nm)
CM	35.45	0.1803	20.34
CM/g-C ₃ N ₄	42.72	0.2092	19.59
C/g-C ₃ N ₄	42.18	0.1992	18.89
M/g-C ₃ N ₄	58.47	0.2041	13.96

3.4. Factors Impacting RhB Degradation by CM/g-C₃N₄/PMS

3.4.1. Catalyst Dosage, PMS Concentration and RhB Concentration

As shown in Figure S2a, the removal efficiency of RhB increased from 36.88 to 99.90% at 5 min, and the k value raised from 0.0867 to 1.2916 min⁻¹ with increasing catalyst dosage (Table S1). More catalysts can provide more reaction sites for PMS activation, thus more active substances can degrade RhB in the reaction system. As shown in Figure S2b, the removal of RhB raised from 91.83 to 99.55% at 5 min for the PMS concentration of 0.50–1.0 mM, with the k value increased from 0.4939 to 1.1703 min⁻¹ (Table S1). As the PMS concentration increased from 1.0 to 3.0 mM, the k value decreased from 1.1703 to 0.8455 min⁻¹. In fact, as the concentration of PMS increases, the activation reaction can be promoted rapidly. However, the self-quenching reaction of PMS will reduce the number of active substances and limit the expression of catalysts due to the overdose of PMS molecules in the reaction system [56]. Figure S2c showed that the degradation efficiency of RhB decreased from 99.90 to 65.69% in the RhB initial concentration range from 5.0 to 20.0 mg/L at 5 min, and the k value dropped from 1.4365 to 0.2187 min⁻¹. This may be because the number of active substances were constant in an assured concentration of catalyst and PMS. The higher the content of RhB, the stronger the competition is among RhB molecules for active substances, which slows down the reaction rate of the CM/g-C₃N₄/PMS system. Considering environmental protection and the concentration of RhB in real life, 0.30 mg/L CM/g-C₃N₄ and 1.0 mM PMS were suitable for 10.0 mg/L RhB degradation.

The k value of the system (0.30 mg/L CM/g-C₃N₄, 1.0 mM PMS, 10.0 mg/L RhB, $k = 1.1703$ min⁻¹) was much higher than those of other reaction systems under the optimal conditions, such as the Fe₃O₄/Co₃S₄/PMS/RhB system (0.302 min⁻¹), 5%-T/LDOs/PMS/RhB system (0.4537 min⁻¹), Co-G/PMS/RhB system (0.9438 min⁻¹) and Co_{1+x}Fe_{2-x}O₄/PMS/RhB system (0.260 min⁻¹) (Table S2). It indicated that CM/g-C₃N₄ can efficiently and rapidly activate PMS to degrade RhB. The mineralization efficiency of RhB in the CM/g-C₃N₄/PMS system reached 43.43% within 5 min and slightly increased (48.93%) in 30 min (Figure S3). It is probable that RhB was decomposed into small molecule intermediates that can undergo sufficient degradation on the surface of CM/g-C₃N₄, then stabilizing the TOC value of the system.

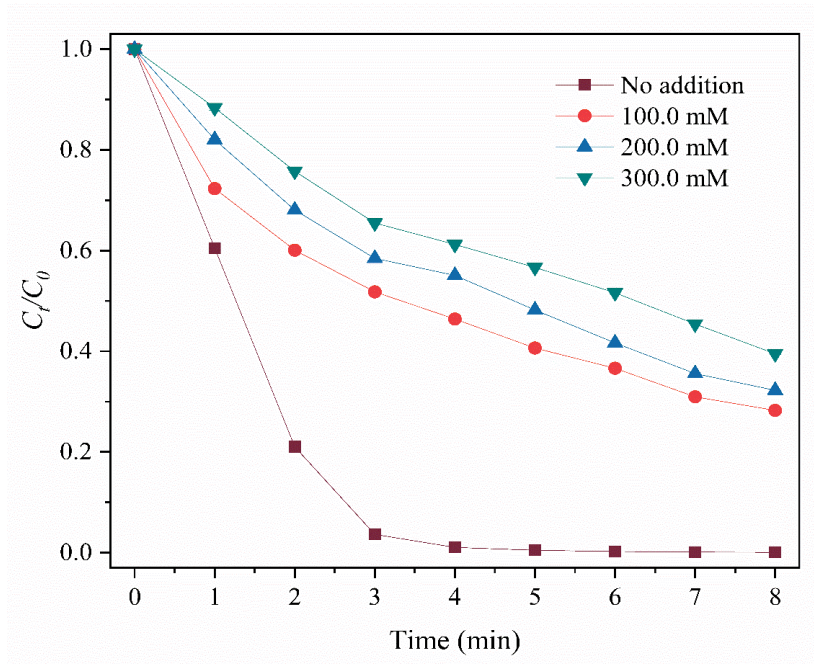
3.4.2. pH

The effects of initial pH (3.0–11.0) on the RhB degradation were investigated under the optimal conditions of 0.30 g/L CM/g-C₃N₄, 1.0 mM PMS and 10.0 mg/L RhB. As shown in Figure S4, the removal of RhB was inhibited under the strong acid (pH = 3.0), weak acid (pH = 5.0) and strong alkaline (pH = 11.0) conditions, with the removal efficiency falling below 40.00% within 6 min. The reason was possible in that PMS was mainly presented in the form of H₂SO₅ (SO₅²⁻) under the acid (strong alkaline) condition [57]. These two forms were not activated by the catalyst to produce active substances for pollutant degradation. Under the neutral (pH = 7.0) and weak alkaline (pH = 9.0) conditions, over 99.00% of RhB was removed in 6 min. This means that the CM/g-C₃N₄/PMS system has good potential for RhB degradation in practical applications because of the neutral or weakly alkaline pH of most actual wastewater.

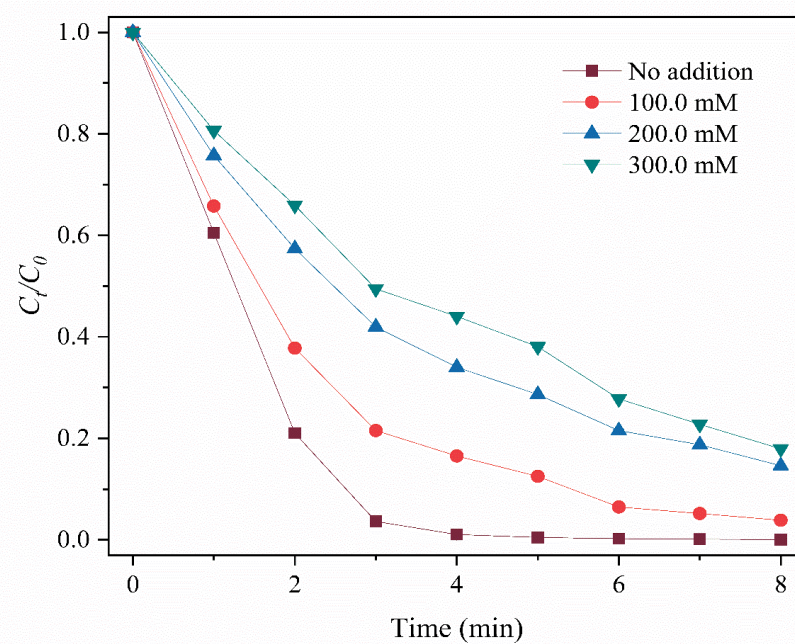
3.5. Possible Activation Mechanisms of PMS

Quenching experiments were utilized to investigate the reactive oxygen species (ROS) produced in the CM/g-C₃N₄/PMS system. Figure 6a,b show that the introduction of MeOH (a scavenger for SO₄^{•-} and •OH) and IPA (a scavenger for •OH) inhibited the removal of RhB. The removal of RhB dropped from 99.88 to 60.50% (MeOH, 300.0 mM) and 82.08% (IPA, 300.0 mM), respectively. Furthermore, the removal efficiency of RhB respectively decreased from 99.88 to 85.78 and 18.14% by adding p-BQ (10.0 mM, O₂^{•-} scavenger) and L-histidine (10.0 mM, ¹O₂ scavenger) into the system (Figure 6c,d). EPR was carried out to verify ROS in the oxidation reactions. As shown in Figure 7a,b, typical signals of DMPO-OH and DMPO-O₂⁻ were respectively observed in the CM/g-C₃N₄/PMS/DMPO and

CM/g-C₃N₄/PMS/DMPO/MeOH systems [40]. However, the DMPO-SO₄^{•-} signal could not be detected in the CM/g-C₃N₄/PMS/DMPO system. It may be because of the low sensitivity and short life of DMPO-SO₄^{•-} signal [39,40,58], but the result of the quenching experiment had shown that SO₄^{•-} existed in the reaction system. A typical TEMP-¹O₂ triplet signal peak with strong intensity was detected in the CM/g-C₃N₄/PMS/TEMP system (Figure 7c), showing the existence of ¹O₂ [59]. All these results indicated that SO₄^{•-}, •OH, O₂^{•-} and ¹O₂ were generated in the CM/g-C₃N₄/PMS system, and both SO₄^{•-} and ¹O₂ were the predominant ROS responsible for the removal of RhB.

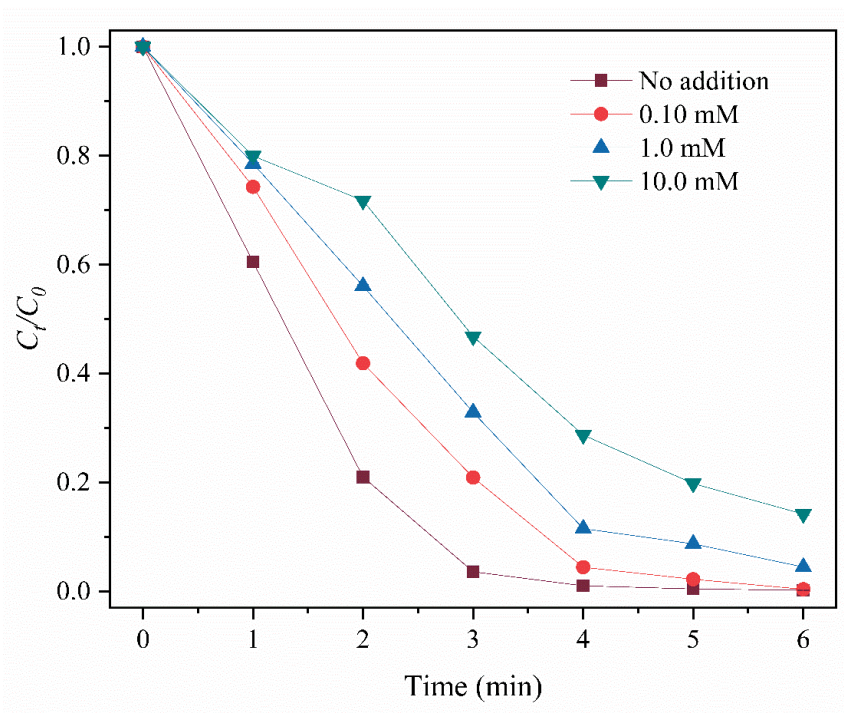


(a)

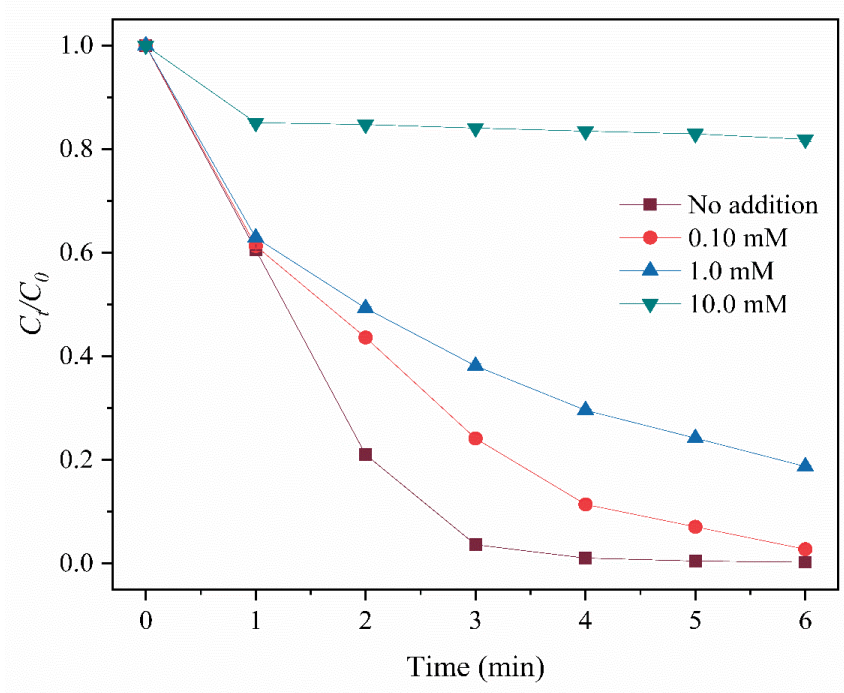


(b)

Figure 6. Cont.



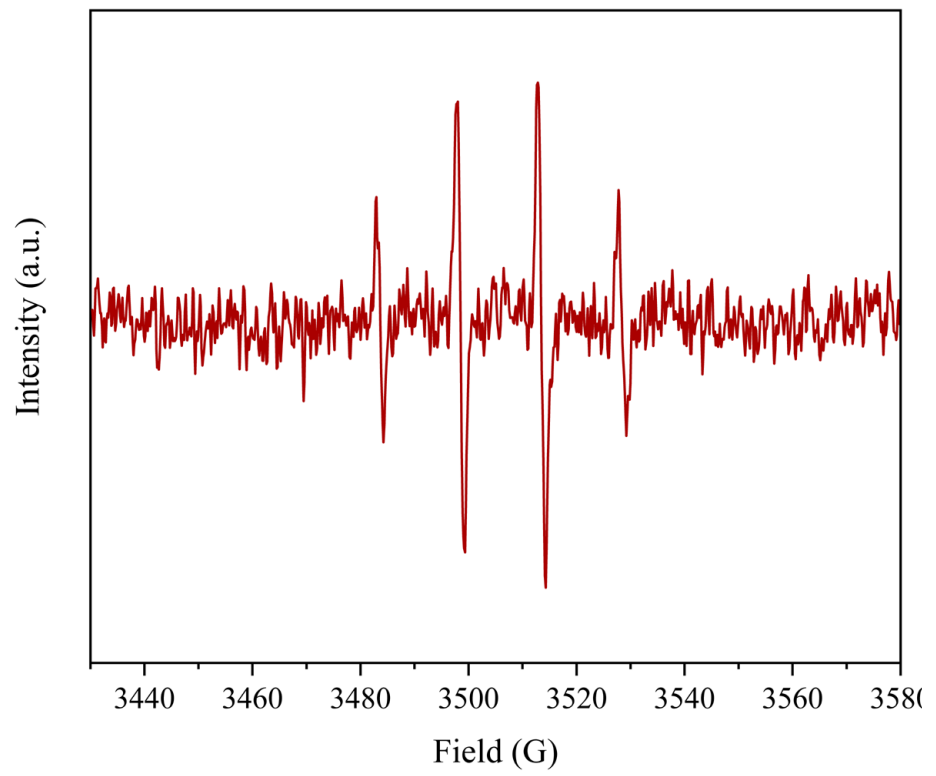
(c)



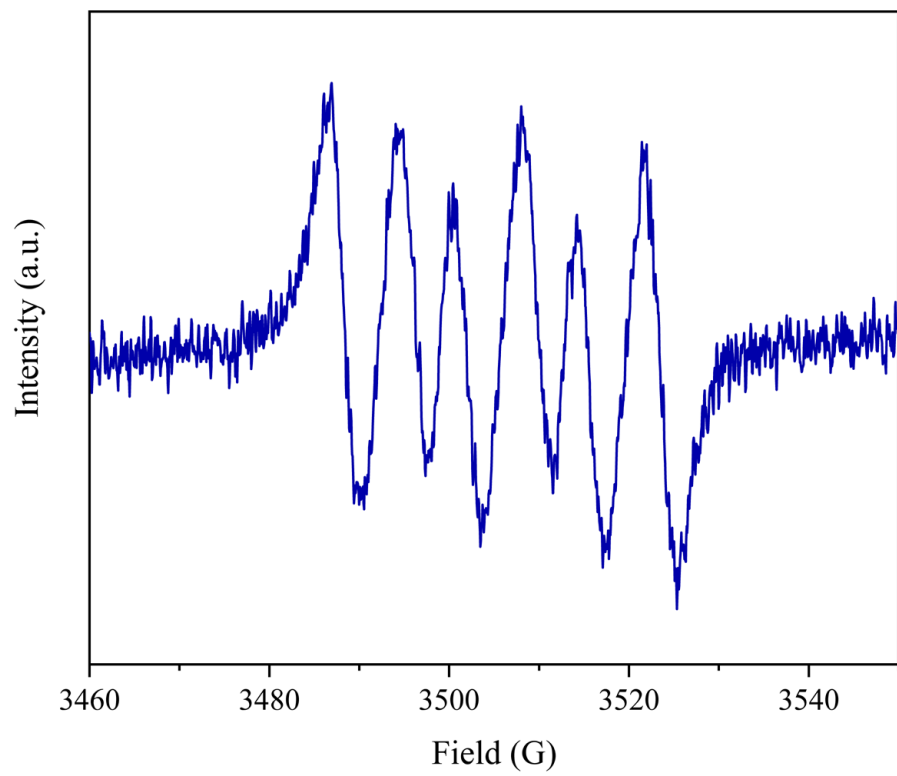
(d)

Figure 6. Effects of different scavengers on RhB removal. MeOH (a), IPA (b), p-BQ (c) and L-Histidine (d). Reaction conditions: [PMS] = 1.0 mM, [CM/g-C₃N₄] = 0.30 g/L, [RhB] = 10.0 mg/L, 25 °C.

The nitrogen was introduced into the CM/g-C₃N₄/PMS system to verify the contribution of dissolved oxygen in the O₂^{•−} generation. As shown in Figure S5, the removal of RhB decreased within 4 min, indicating that dissolved oxygen had contributed to O₂^{•−} generation to some extent.



(a)



(b)

Figure 7. Cont.

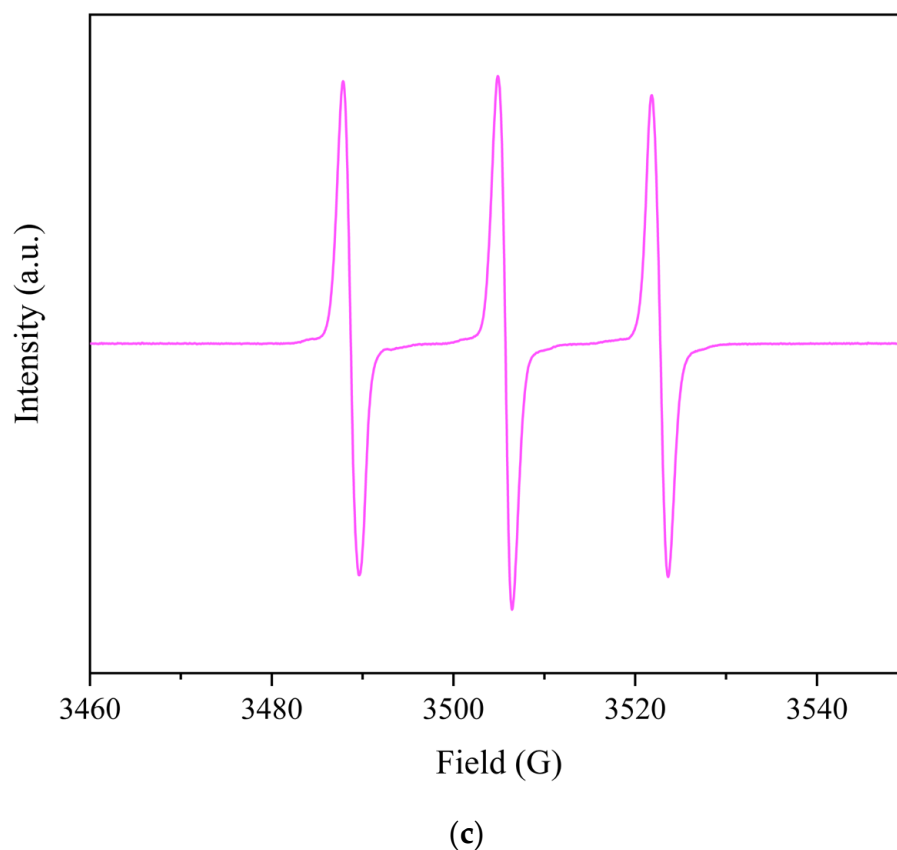
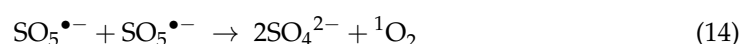
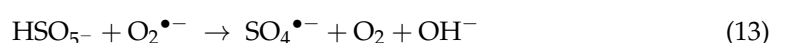
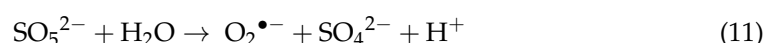
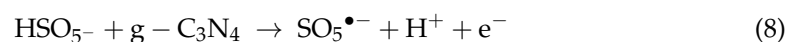
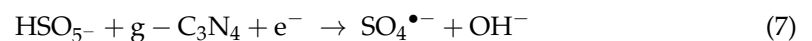
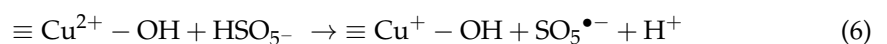
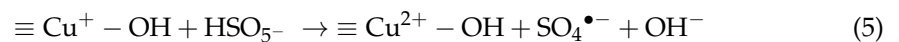


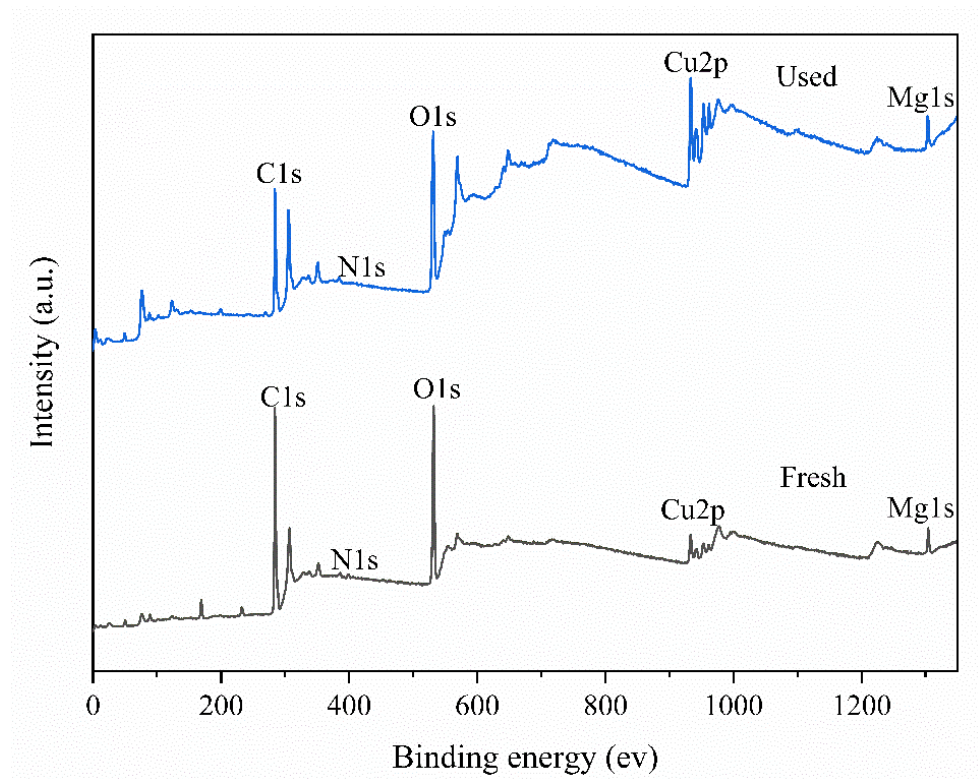
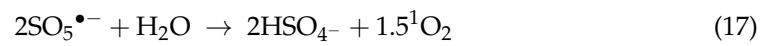
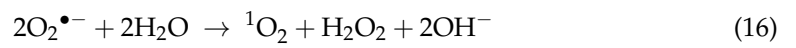
Figure 7. EPR spectra of $\text{SO}_4^{\bullet-}$ and $\bullet\text{OH}$ (a), $\text{O}_2^{\bullet-}$ (b) and $^1\text{O}_2$ (c) in the CM/g- C_3N_4 /PMS system. Reaction conditions: [PMS] = 1.0 mM, [CM/g- C_3N_4] = 0.30 g/L, [RhB] = 10.0 mg/L, DMPO/TEMP = 0.10 M, 25 °C.

In order to clarify the surface components of CM/g- C_3N_4 before and after the reaction, XPS analysis was performed, and the atomic area ratios of different components were shown in Table S3. The full spectrum shows that CM/g- C_3N_4 contained C, O, N, Cu and Mg elements, and there was little difference in its spectrum before and after the reaction (Figure 8a), showing the stability of CM/g- C_3N_4 . The C1s spectrum showed three peaks at 284.8 (C–C), 286.47 (C–O) and 288.72 eV (C=O) (Figure S6a,b). The atomic area ratios of C–C, C–O and C=O before (after) the reaction were 79.00 (77.42%), 11.68 (10.4%) and 9.32% (12.18%), respectively (Table S3). The result indicates that C–O may participate in the activation process of PMS. For O1s' spectrum, three binding energy peaks at 529.91, 531.93 and 532.84 eV could be classified as lattice oxygen (O^{2-}), hydroxyl groups (–OH) and adsorbed oxygen [60,61], with atomic area ratios of 9.58, 43.27 and 41.99%, respectively (Figure 8b, Table S3). After the reaction, the atomic area ratios of O^{2-} and –OH increased to 25.14 and 45.79%, with adsorbed oxygen being reduced to 13.78% (Figure 8c, Table S3). The result demonstrates that adsorbed oxygen was important for PMS activation. Adsorbed oxygen can promote the formation of –OH on the surface of the catalyst and facilitate the activation of PMS [62,63]. Previous studies have shown that –OH is an important reaction site for PMS activation, and H_2PO_4^- has a strong chelating influence on the –OH of catalyst surfaces [64–66], thus impacting the PMS activation. Therefore, H_2PO_4^- was introduced into the CM/g- C_3N_4 /PMS system to investigate the role of –OH. As shown in Figure S7, the RhB removal was inhibited at the H_2PO_4^- concentration of 1.0–8.0 mM at 4 min. This indicated that –OH on the CM/g- C_3N_4 surface was an important reaction site for PMS activation. Hence, the adsorbed oxygen on the surface of CM/g- C_3N_4 can provide more reaction sites for activating PMS. The higher atomic area ratio of –OH after the reaction demonstrated that the rate of consuming –OH was slower than that of producing –OH. This

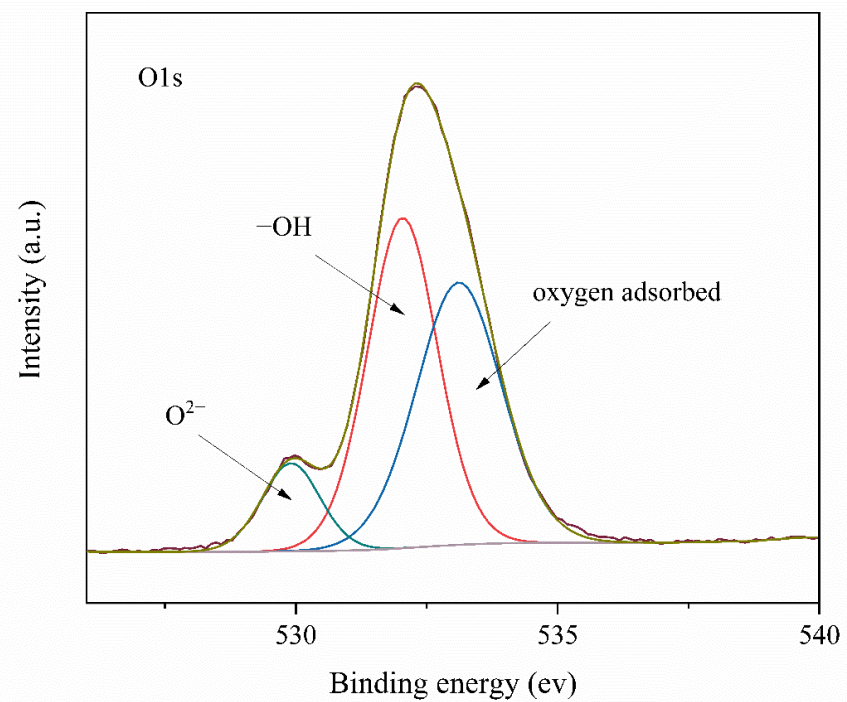
is mainly because of the constant formation of –OH by adsorbed oxygen. For N1s' spectrum, two peaks with the binding energy of 398.7 and 400.6 eV were related to sp^2 hybridized N atoms (C=N–C) and N(C)³ groups (C–N), respectively (Figure 8d,e) [45]. The atomic area ratio of C=N–C groups decreased from 86.45 to 40.03%, and that of C–N groups increased from 13.55 to 59.97% (Table S1). This shows that the g-C₃N₄ of CM/g-C₃N₄ has an important contribution to PMS activation, and the conversion of copper species on the surface of g-C₃N₄ may occur [63]. For the Cu2p spectrum, the binding peaks located at 933.12 and 934.41 eV could be respectively ascribed to Cu⁺ and Cu²⁺ [40,62], with atomic area ratios of 42.59 and 57.41% (Figure 8f, Table S1). After the reaction, the atomic area ratios of Cu⁺ and Cu²⁺ were 51.14 and 48.86% respectively (Figure 8g, Table S1), indicating that the conversion between Cu⁺ and Cu²⁺ were a major factor in activating PMS. For Mg1s' spectrum, the binding energy peak before and after the reaction was at 1304.59 ± 0.5 eV (Figure S6c,d). It is a typical MgO peak.

Based on the above analyses, the possible activation mechanism of PMS by CM/g-C₃N₄ could be sufficiently expressed by Equations (3)–(17) (Scheme 1). They show the redox cycle of Cu²⁺/Cu⁺-activated PMS to produce SO₄^{•-}, OH⁻ and SO₅^{•-} (Equations (3) and (4)). The results of FTIR and XPS analyses had shown that the interaction between MgO and g-C₃N₄ and the adsorbed oxygen on the surface of CM/g-C₃N₄ would enhance the production of –OH, which promoted the formation of Cu–OH complexes. PMS could react with these substances to form SO₄^{•-} and SO₅^{•-} (Equations (5) and (6)) [67]. The results of RhB removed by the g-C₃N₄/PMS system and XPS analysis had indicated that g-C₃N₄ was not only a supporter but also participated in the PMS activation. The electron-rich structure of g-C₃N₄ could provide electrons to promote the reduction of PMS. Moreover, PMS could act as an electron donor due to the presence of O–O bonds and the C atoms adjacent to the N atoms in g-C₃N₄ could act as the electron acceptors (Equations (7) and (8)) [68]. The generated SO₄^{•-} reacted with water molecules or OH⁻ to produce •OH (Equation (9)). In the oxidation system, PMS would be hydrolyzed to produce O₂^{•-} [40]. Furthermore, as mentioned earlier, dissolved oxygen also contributed to O₂^{•-} generation (Equations (10) and (12)). The generated O₂^{•-} could consume PMS to accelerate the production of SO₄^{•-} for improving the oxidation performance of system (Equation (13)). The self-reaction of SO₅^{•-} generated in the PMS activation and the self-decomposition of PMS would produce ¹O₂ (Equations (14) and (15)) [69]. Moreover, the reaction between O₂^{•-} (SO₅^{•-}) and water molecules would also generate ¹O₂ (Equations (16) and (17)) [70–72]. RhB was transformed into small molecule intermediates and finally mineralized into H₂O and CO₂ under the action of SO₄^{•-}, •OH, O₂^{•-} and ¹O₂.



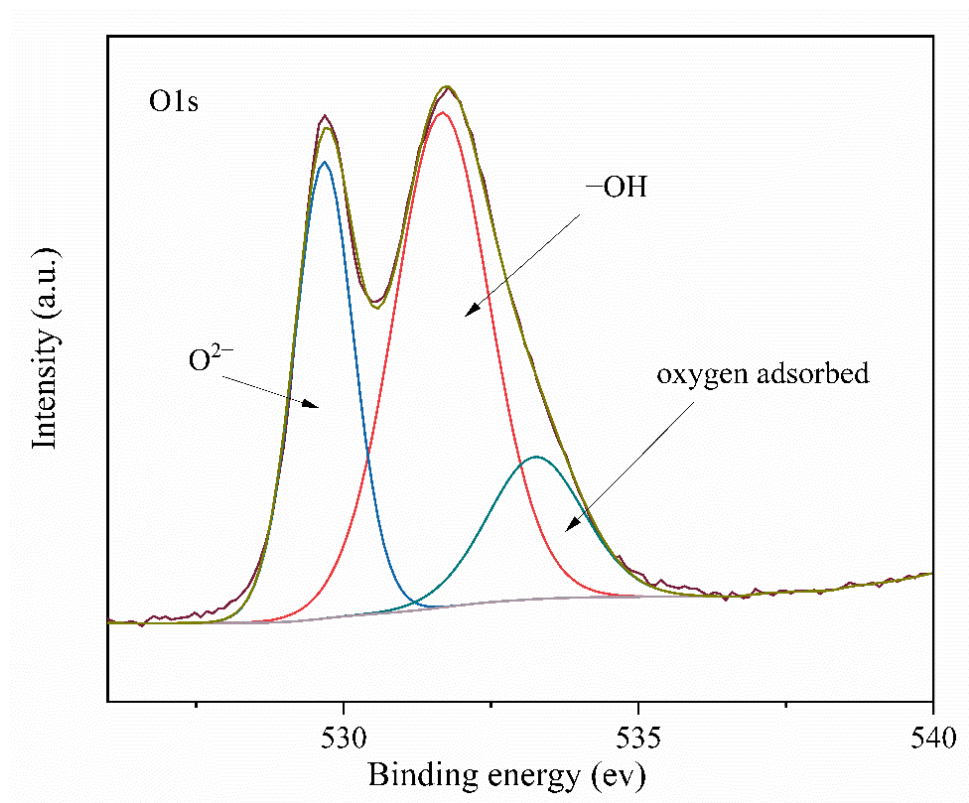


(a)

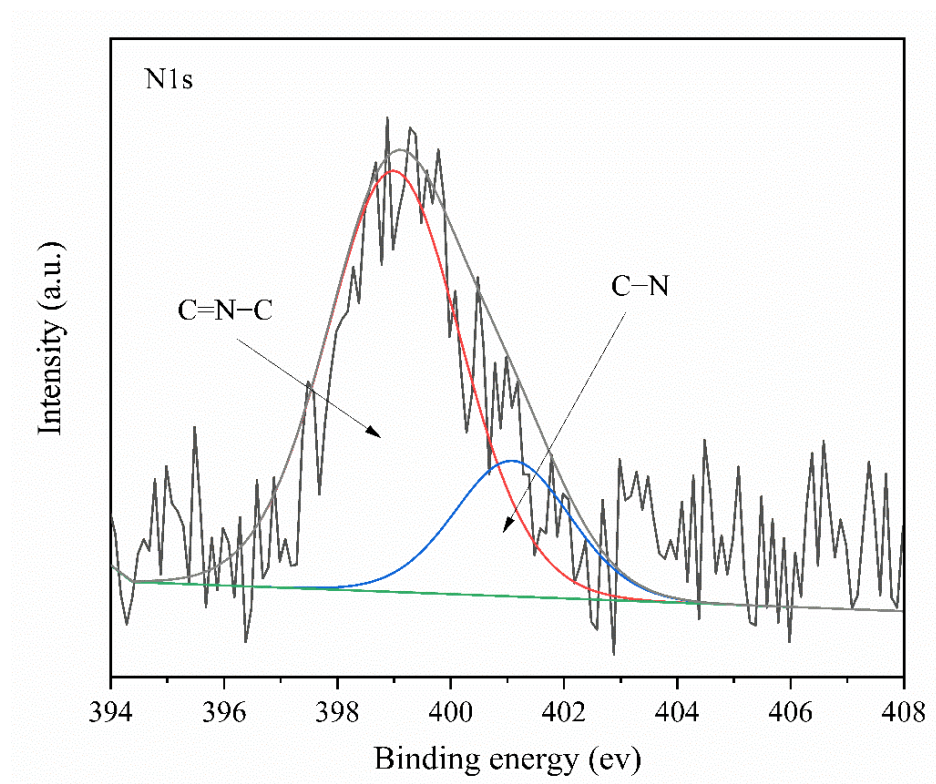


(b)

Figure 8. Cont.

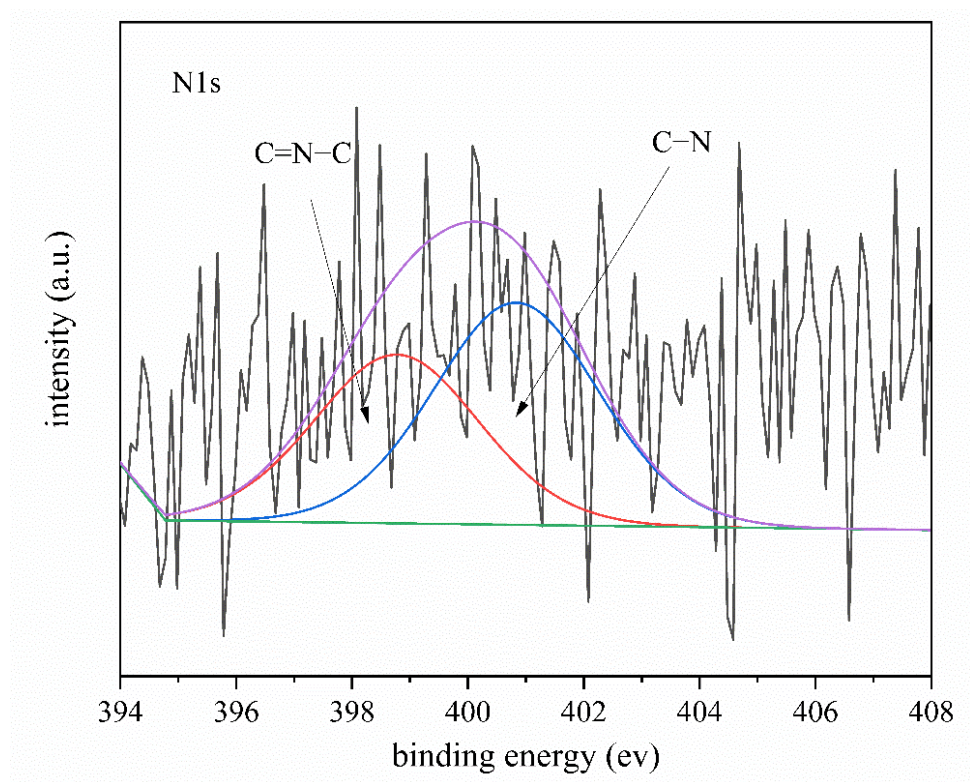


(c)

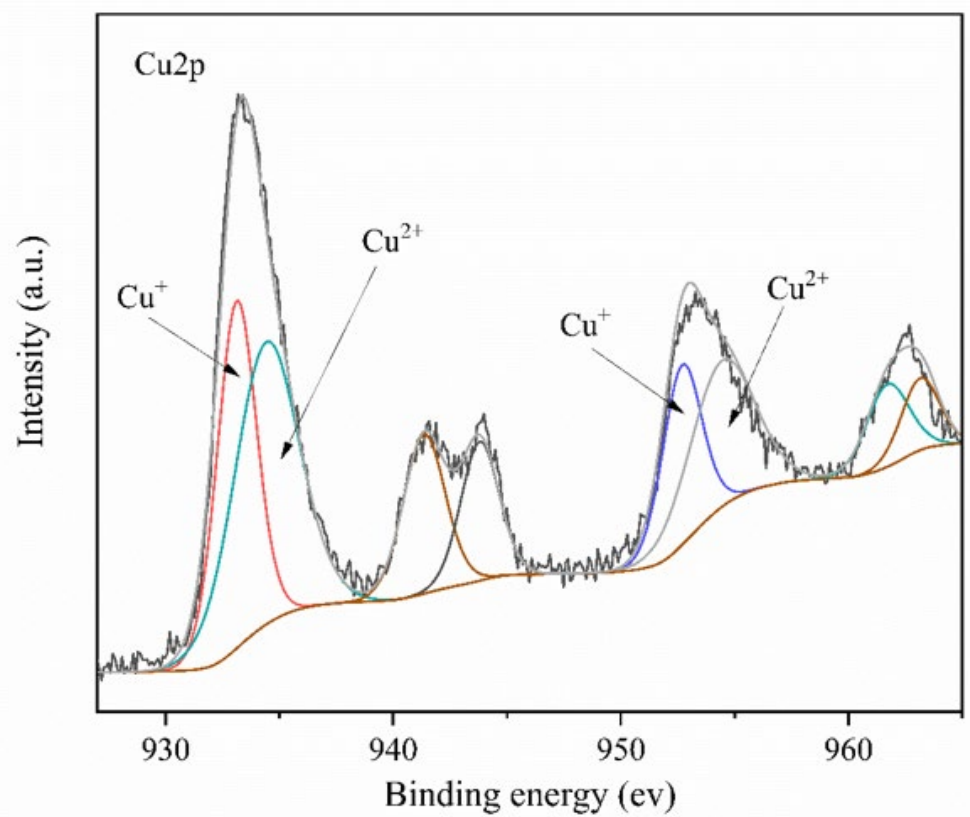


(d)

Figure 8. Cont.



(e)



(f)

Figure 8. Cont.

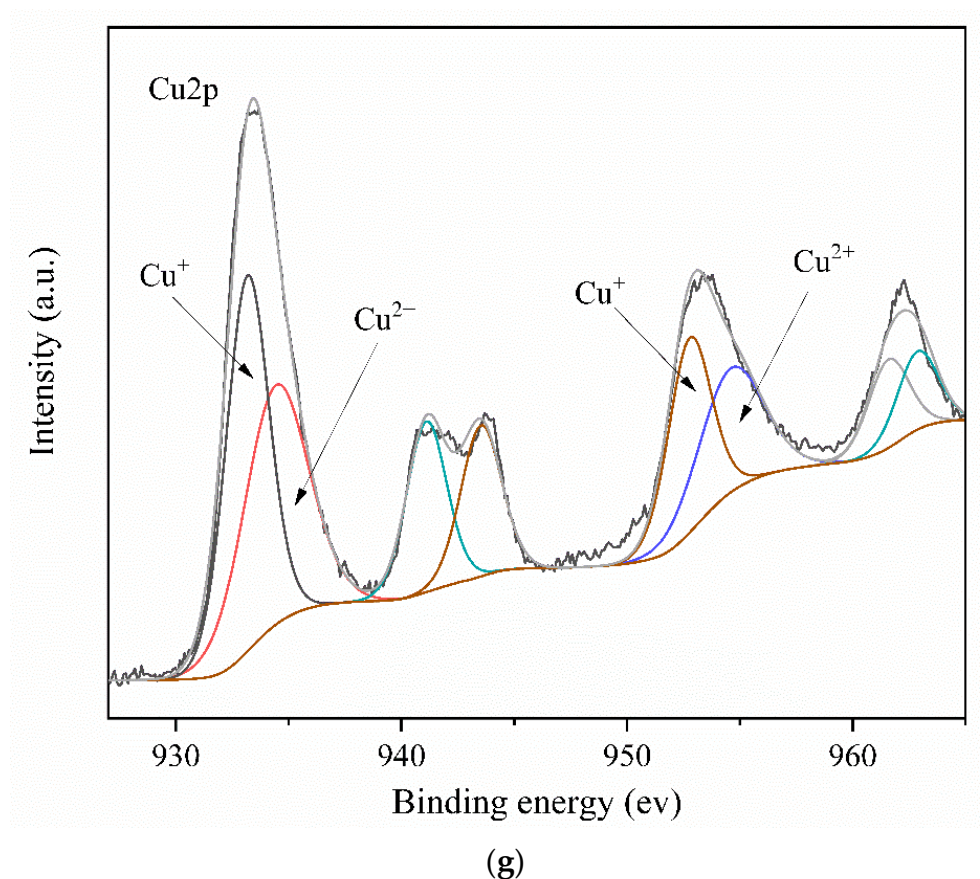
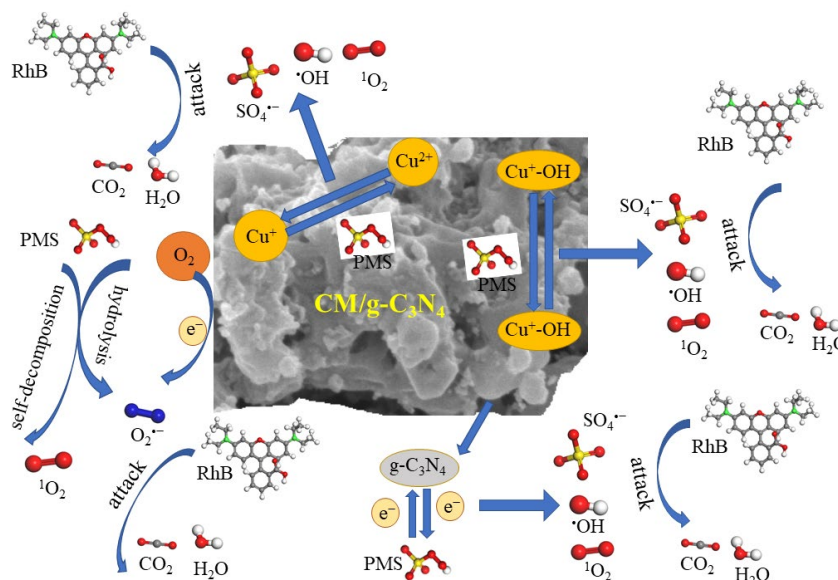


Figure 8. X-ray photoelectron spectroscopy spectra of full survey (a), O1s (b,c), N 1s (d,e), Cu 2p (f,g) in the CM/g-C₃N₄ before (b,d,f) and after (c,e,g) the reaction.



Scheme 1. The possible activation mechanism of PMS.

3.6. Degradation Pathway of RhB and Toxicity Estimation

The oxidation intermediates of RhB were detected by LC-MS analysis. Generally, the degradation of RhB occurs through a series of reactions, including N-demethylation, deamination, dealkylation, decarboxylation, chromophore cleavage, ring-opening and mineralization [73–75]. The DFT calculation was used to analyze the molecular structure

of RhB (Figure S8). The result indicated that C10 was vulnerable to being attacked by active substances, and the atoms shown in Table S4 were also under attack. Depending on the previous reports, the LC-MS analysis and the DFT calculation, nineteen intermediates including isomers were identified during the reaction [75–84]. As shown in Figure 9, the degradation pathway of RhB in the CM/g-C₃N₄/PMS system was proposed. First, under the intense attack of various active species, RhB ($m/z = 443$) was transformed into a series of intermediates (P1–P6) by N-demethylation and deamination. Then, P7 and P8 intermediates were produced by the decarboxylation and further oxidation of P6. Moreover, the chromophores of intermediates (P1–P8) were cleaved to form the P9–P13 intermediates. By a ring-opening reaction, the P9–P13 intermediates further formed small molecule products (P14–P19). Finally, RhB and its intermediates were mineralized into CO₂ and H₂O. Many small intermediates of RhB were produced in the CM/g-C₃N₄/PMS system, showing the good degradation capacity of this system.

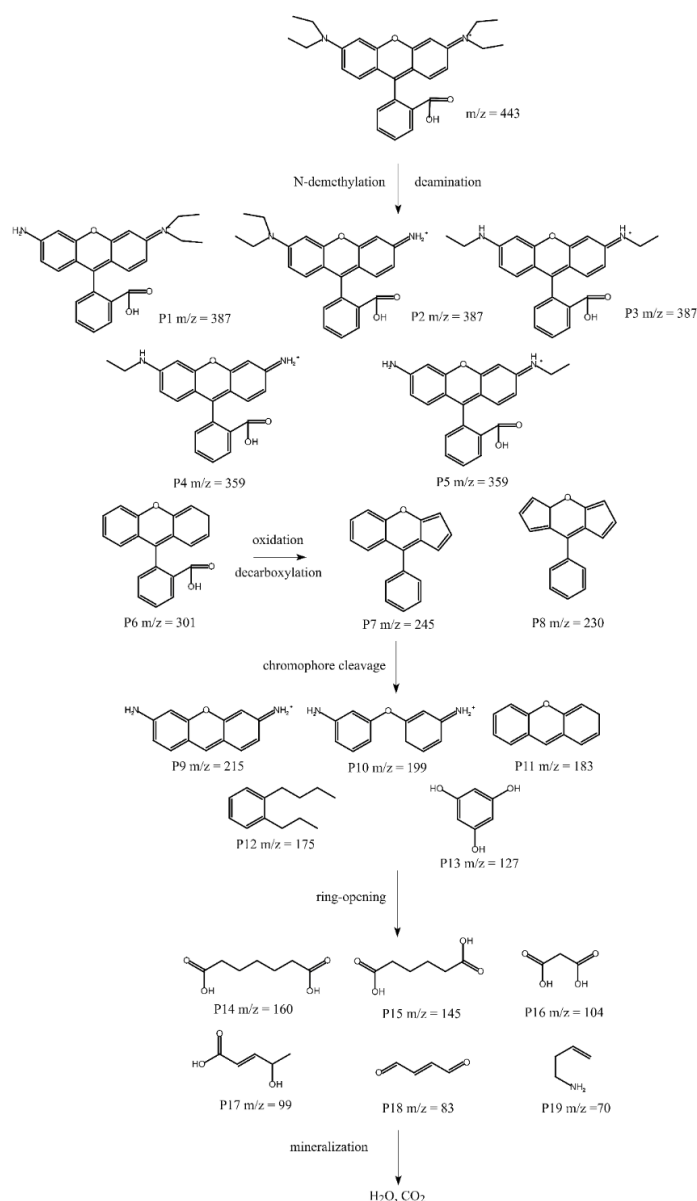


Figure 9. Proposed degradation pathway of RhB in the CM/g-C₃N₄/PMS system.

The toxicity estimation is important for predicting the damage of pollutants to the environment and humans. Therefore, the toxicities of RhB and its intermediates were

examined by assessing oral rat LD₅₀ and bioaccumulation factors on the TEST. The results are shown in the Figure 10. The predicted oral rat LD₅₀ of RhB was 924.86 mg/kg. Except for P5, P7 and P19, the oral rat LD₅₀ of other intermediates decreased after the degradation of RhB, indicating that the toxicities of intermediates were reduced. The predicted bioaccumulation factor was 15.48 in the RhB, and decreased significantly in the intermediates, indicating the lower accumulation of intermediates in the organisms. In terms of oral rat LD₅₀ and bioaccumulation factors, the CM/g-C₃N₄/PMS system was able to sufficiently reduce RhB toxicity by transforming it into a series of intermediates with lower toxicity.

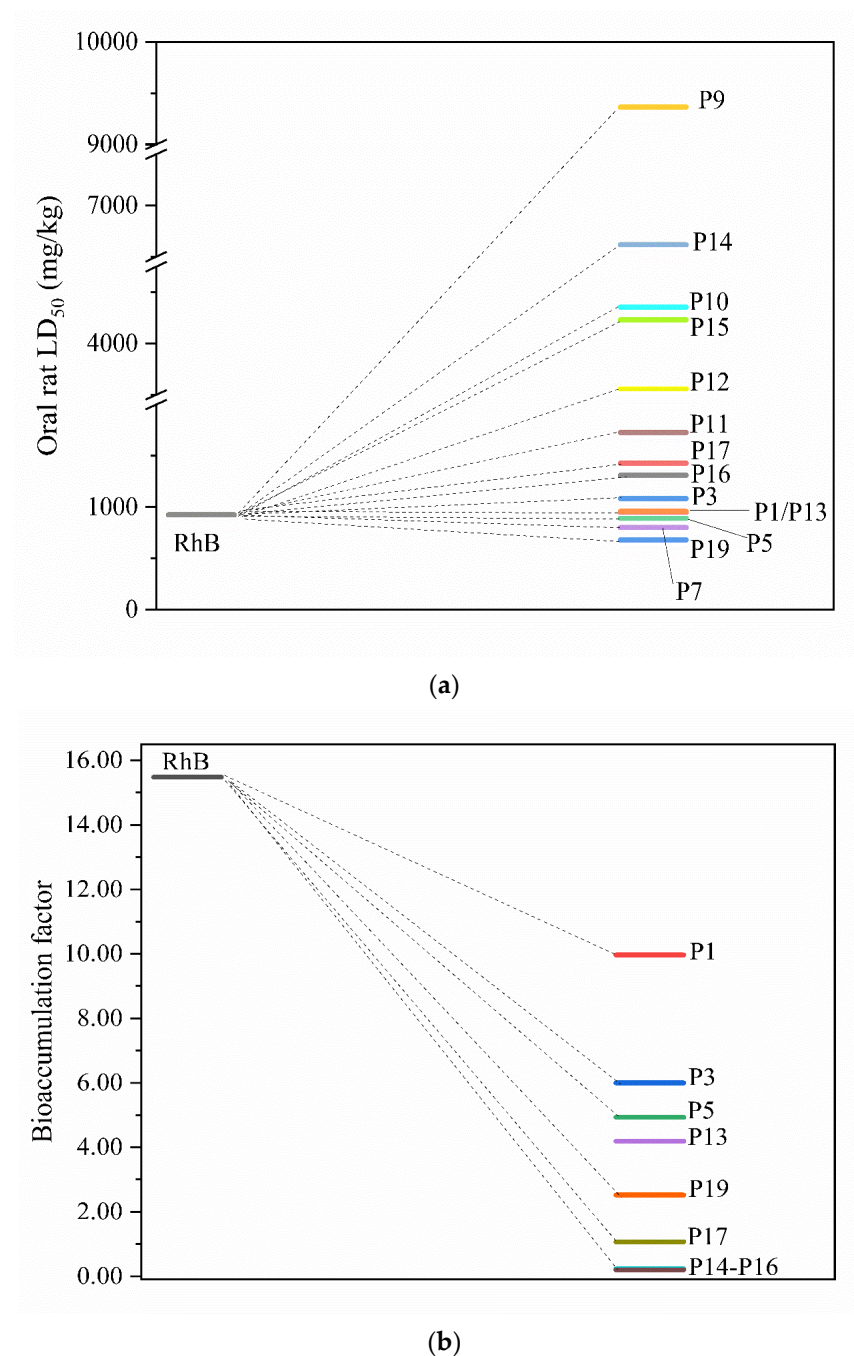


Figure 10. Oral rat LD₅₀ (a) and bioaccumulation factors (b) of RhB and its intermediates.

3.7. Stability of the CM/g-C₃N₄

The stability and repeatability of a material is an important parameter to measure its practical applications. Therefore, the CM/g-C₃N₄ was reused five times under the same

conditions (0.30 g/L CM/g-C₃N₄, 1.0 mM PMS, 10.0 mg/L RhB). As shown in Figure S9, the removal of RhB decreased from 99.88 to 99.30% after five cycles, showing the good repeatability of CM/g-C₃N₄. This indicates that the CM/g-C₃N₄ was stable for long-term running. The leaching concentrations of copper and magnesium ions were monitored by ICP-OES. The results showed that the loss of copper and magnesium ions were 5.16 and 31.97 mg/L after the reaction, respectively. As a non-toxic metal, magnesium ions are widely present in the water matrix with a concentration of about 0.0–130.0 mg/L. Unlike transition metal ions, the leaching of magnesium ions would not cause secondary pollution. In addition, the copper ion leaching concentration of CM/g-C₃N₄ was lower than those of other copper-based heterogeneous catalysts (Cu₂FeSnS₄ (16.70 mg/L), such as Cu₂S (131.60 mg/L) [85]). All the above results show that the eco-friendly and stable CM/g-C₃N₄ system has great application potential in the field of environmental remediation.

3.8. Practical Application of the CM/g-C₃N₄/PMS System

The CM/g-C₃N₄/PMS system could degrade other pollutants, such as CR, MB and TC (Figure 11a). The removal of CR, MB and TC were all over 73.00%, indicating that the CM/g-C₃N₄/PMS system can oxidize various contaminants. Figure 11b reveals that RhB could be degraded in the tap water and the wastewater in 10 min, indicating that the CM/g-C₃N₄/PMS system can efficiently remove RhB in the actual environment. All these results indicate that the CM/g-C₃N₄ system has the practical application potential for pollutant degradation.

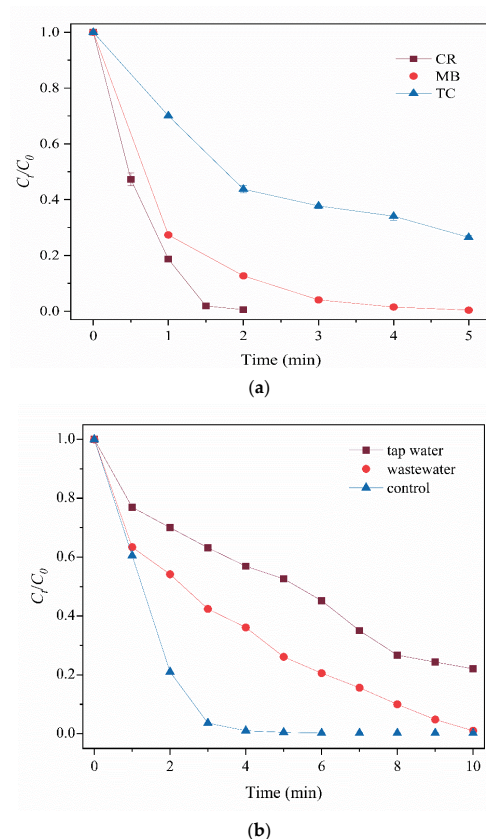


Figure 11. Degradation of different pollutants in the CM/g-C₃N₄/PMS system (a) and RhB removal in different water matrixes (b). Reaction conditions: [PMS] = 1.0 mM, [CM/g-C₃N₄] = 0.30 g/L, [RhB/CR/MB/TC] = 10.0 mg/L, 25 °C.

4. Conclusions

CM/g-C₃N₄ was synthesized and initially used as a heterogeneous catalyst to activate PMS for the degradation of RhB. Owing to the splendid structure and abundant reaction

sites, CM/g-C₃N₄ exhibited much a better catalytic performance than CuO, CM, g-C₃N₄, M/g-C₃N₄ and C/g-C₃N₄. Under the low usage reaction conditions, RhB could be rapidly degraded at a natural pH in 5 min. PMS was activated by the copper and g-C₃N₄ in CM/g-C₃N₄, with SO₄^{•−} and ¹O₂ as the main active substances for the removal of RhB. CM/g-C₃N₄ showed good stability and reusability. This work enriches the family of copper-based heterogeneous catalysts used in the PMS activation, and provides a guiding role of enhancing the catalytic performance of copper oxide. The copper-based catalyst with a higher specific surface area, used for industrial applications, should be considered in the future work.

Supplementary Materials: The following supporting information can be downloaded at: <https://www.mdpi.com/article/10.3390/w14132054/s1>. Scheme S1: Preparation of CM/g-C₃N₄. Figure S1: Effects of different g-C₃N₄ precursors (a), mass ratios of copper-magnesium oxide to melamine (b), pyrolysis temperatures (c), pyrolysis times (d) and molar ratios of copper to magnesium precursor (e) on the catalytic performance of material. Figure S2: Effects of catalyst dosage (a), PMS concentration (b) and RhB concentration (c) for RhB degradation. Figure S3: Mineralization efficiency of CM/g-C₃N₄/PMS system. Figure S4: Effect of initial pH for RhB degradation in the CM/g-C₃N₄/PMS system. Figure S5: Effect of nitrogen on the degradation of RhB in the CM/g-C₃N₄/PMS system. Figure S6: X-ray photoelectron spectroscopy spectra of C1s (a, b) and Mg 1s (c, d) in the CM/g-C₃N₄ before (a, c) and after (b, d) the reaction. Figure S7: Effect of H₂PO₄[−] on the degradation of RhB in the CM/g-C₃N₄/PMS system. Figure S8: The molecular structure of the optimized RhB (a) (oxygen, red; carbon, gray; nitrogen, green; hydrogen, white). Figure S9: Degradation of RhB with the recycled CM/g-C₃N₄. Figure S10: Degradation of different pollutants in the CM/g-C₃N₄/PMS system (a) and RhB removal in different water matrixes (b). Table S1: k value of CM/g-C₃N₄/PMS system in different conditions. Table S2: RhB degradation in different systems. Table S3: Atomic area ratios of different compositions in the CM/g-C₃N₄ before and after the reaction. Table S4: Partial Fukui indexes of RhB molecule.

Author Contributions: Conceptualization, Y.M.; Formal analysis, Y.M.; Funding acquisition, X.Z.; Methodology, W.X.; Project administration, X.Z.; Resources, X.Z.; Software, W.X.; Supervision, X.Z. and S.Z.; Writing—original draft, Y.M.; Writing—review & editing, X.Z. All authors have read and agreed to the published version of the manuscript.

Funding: This research was funded by the National Key Research and Development Program of China, (Grant No. 2016YFC0400702-2), the National Natural Science Foundation of China (Grant No. 21377041) and the Guangdong Science and Technology Program (Grant No.2020B121201003).

Institutional Review Board Statement: Not applicable.

Informed Consent Statement: Not applicable.

Data Availability Statement: Not applicable.

Conflicts of Interest: The authors declare that they have no known competing financial interests or personal relationships that could have appeared to influence the work reported in this paper.

References

1. Solis, M.; Solis, A.; Ines Perez, H.; Manjarrez, N.; Flores, M. Microbial decolouration of azo dyes: A review. *Process Biochem.* **2012**, *47*, 1723–1748. [[CrossRef](#)]
2. Ren, Q.; Nie, M.; Yang, L.; Wei, F.; Ding, B.; Chen, H.; Liu, Z.; Liang, Z. Synthesis of MOFs for RhB Adsorption from Wastewater. *Inorganics* **2022**, *10*, 27. [[CrossRef](#)]
3. Sivarajasekar, N.; Baskar, R. Agriculture waste biomass valorisation for cationic dyes sequestration: A concise review. *J. Chem. Pharm. Res.* **2015**, *7*, 737–748.
4. Shi, X.; Hong, P.; Huang, H.; Yang, D.; Zhang, K.; He, J.; Li, Y.; Wu, Z.; Xie, C.; Liu, J.; et al. Enhanced peroxymonosulfate activation by hierarchical porous Fe₃O₄/Co₃S₄ nanosheets for efficient elimination of rhodamine B: Mechanisms, degradation pathways and toxicological analysis. *J. Colloid Interface Sci.* **2022**, *610*, 751–765. [[CrossRef](#)]
5. Yang, S.; Zhang, S.; Li, X.; Du, Y.; Xing, Y.; Xu, Q.; Wang, Z.; Li, L.; Zhu, X. One-step pyrolysis for the preparation of sulfur-doped biochar loaded with iron nanoparticles as an effective peroxymonosulfate activator for RhB degradation. *New J. Chem.* **2022**, *46*, 5678–5689. [[CrossRef](#)]

6. Foo, K.Y.; Hameed, B.H. Decontamination of textile wastewater via TiO₂/activated carbon composite materials. *Adv. Colloid Interface Sci.* **2010**, *159*, 130–143. [\[CrossRef\]](#)
7. Noman, E.; Al-Gheethi, A.A.; Talip, B.; Mohamed, R.; Kassim, A.H. Mycoremediation of Remazol Brilliant Blue R in greywater by a novel local strain of *Aspergillus iizukae* 605EAN: Optimisation and mechanism study. *Int. J. Environ. Anal. Chem.* **2020**, *100*, 1650–1668. [\[CrossRef\]](#)
8. Yousefi, S.; Ghanbari, D.; Salavati-Niasari, M.; Hassanpour, M. Photo-degradation of organic dyes: Simple chemical synthesis of Ni(OH)₂ nanoparticles, Ni/Ni(OH)₂ and Ni/NiO magnetic nanocomposites. *J. Mater. Sci.-Mater. Electron.* **2016**, *27*, 1244–1253. [\[CrossRef\]](#)
9. Yang, Q.; Zhang, Y.; Liang, J.; Luo, Y.; Liu, Q.; Yang, Y.; Sun, X. Facile hydrothermal synthesis of co-glycerate as an efficient peroxymonosulfate activator for rhodamine B degradation. *Colloids Surf. A-Physicochem. Eng. Asp.* **2022**, *648*, 129239. [\[CrossRef\]](#)
10. Yousefi, S.; Alshamsi, H.; Amiri, O.; Salavati-Niasari, M. Synthesis, characterization and application of Co/Co₃O₄ nanocomposites as an effective photocatalyst for discoloration of organic dye contaminants in wastewater and antibacterial properties. *J. Mol. Liq.* **2021**, *337*, 116405. [\[CrossRef\]](#)
11. Syuhei, Y.; Kohei, M.; Hidenori, Y. Catalytic oxidation of benzene to phenol with hydrogen peroxide over Fe-terpyridine complexes supported on a cation exchange resin. *Catal. Commun.* **2018**, *116*, S1566736718303224.
12. Amanollahi, H.; Moussavi, G.; Giannakis, S. Enhanced vacuum UV-based process (VUV/H₂O₂/PMS) for the effective removal of ammonia from water: Engineering configuration and mechanistic considerations. *J. Hazard. Mater.* **2021**, *402*, 123789. [\[CrossRef\]](#)
13. Duan, X.; Sun, H.; Shao, Z.; Wang, S. Nonradical reactions in environmental remediation processes: Uncertainty and challenges. *Appl. Catal. B Environ.* **2018**, *224*, 973–982. [\[CrossRef\]](#)
14. Ling, S.K.; Wang, S.; Peng, Y. Oxidative degradation of dyes in water using Co²⁺/H₂O₂ and Co²⁺/peroxymonosulfate. *J. Hazard. Mater.* **2010**, *178*, 385–389. [\[CrossRef\]](#)
15. Rodriguez-Narvaez, O.M.; Pacheco-Alvarez, M.O.A.; Wrobel, K.; Paramo-Vargas, J.; Bandala, E.R.; Brillas, E.; Peralta-Hernandez, J.M. Development of a Co²⁺/PMS process involving target contaminant degradation and PMS decomposition. *Int. J. Environ. Sci. Technol.* **2020**, *17*, 17–26. [\[CrossRef\]](#)
16. Ulucan-Altuntas, K.; Guvenc, S.Y.; Can-Guven, E.; Ilhan, F.; Varank, G. Degradation of oxytetracycline in aqueous solution by heat-activated peroxydisulfate and peroxymonosulfate oxidation. *Environ. Sci. Pollut. Res.* **2022**, *29*, 9110–9123. [\[CrossRef\]](#)
17. Huang, S.; Guo, X.; Duan, W.; Cheng, X.; Zhang, X.; Li, Z. Degradation of high molecular weight polyacrylamide by alkali-activated persulfate: Reactivity and potential application in filter cake removal before cementing. *J. Pet. Sci. Eng.* **2019**, *174*, 70–79. [\[CrossRef\]](#)
18. Yin, R.; Guo, W.; Wang, H.; Du, J.; Zhou, X.; Wu, Q.; Zheng, H.; Chang, J.; Ren, N. Enhanced peroxymonosulfate activation for sulfamethazine degradation by ultrasound irradiation: Performances and mechanisms. *Chem. Eng. J.* **2018**, *335*, 145–153. [\[CrossRef\]](#)
19. Cui, C.; Jin, L.; Jiang, L.; Han, Q.; Lin, K.; Lu, S.; Zhang, D.; Cao, G. Removal of trace level amounts of twelve sulfonamides from drinking water by UV-activated peroxymonosulfate. *Sci. Total Environ.* **2016**, *572*, 244–251. [\[CrossRef\]](#)
20. Li, T.; Du, X.; Deng, J.; Qi, K.; Zhang, J.; Gao, L.; Yue, X. Efficient degradation of Rhodamine B by magnetically recoverable Fe₃O₄-modified ternary CoFeCu-layered double hydroxides via activating peroxymonosulfate. *J. Environ. Sci.* **2021**, *108*, 188–200. [\[CrossRef\]](#)
21. Wan, Q.; Chen, Z.; Cao, R.; Wang, J.; Huang, T.; Wen, G.; Ma, J. Oxidation of organic compounds by PMS/CuO system: The significant discrepancy in borate and phosphate buffer. *J. Clean. Prod.* **2022**, *339*, 130773. [\[CrossRef\]](#)
22. Deng, J.; Ya, C.; Ge, Y.; Cheng, Y.; Chen, Y.; Xu, M.; Wang, H. Activation of peroxymonosulfate by metal (Fe, Mn, Cu and Ni) doping ordered mesoporous Co₃O₄ for the degradation of enrofloxacin. *Rsc Adv.* **2018**, *8*, 2338–2349. [\[CrossRef\]](#)
23. He, Y.; Zhang, J.; Zhou, H.; Yao, G.; Lai, B. Synergistic multiple active species for the degradation of sulfamethoxazole by peroxymonosulfate in the presence of CuO@FeOx@Fe-0. *Chem. Eng. J.* **2020**, *380*, 122568. [\[CrossRef\]](#)
24. Li, W.; Li, Y.; Zhang, D.; Lan, Y.; Guo, J. CuO-Co₃O₄@CeO₂ as a heterogeneous catalyst for efficient degradation of 2,4-dichlorophenoxyacetic acid by peroxymonosulfate. *J. Hazard. Mater.* **2020**, *381*, 122568. [\[CrossRef\]](#)
25. Ji, F.; Li, C.; Liu, Y.; Liu, P. Heterogeneous activation of peroxymonosulfate by Cu/ZSM5 for decolorization of Rhodamine B. *Sep. Purif. Technol.* **2014**, *135*, 1–6. [\[CrossRef\]](#)
26. Du, X.; Zhang, Y.; Si, F.; Yao, C.; Du, M.; Hussain, I.; Kim, H.; Huang, S.; Lin, Z.; Hayat, W. Persulfate non-radical activation by nano-CuO for efficient removal of chlorinated organic compounds: Reduced graphene oxide-assisted and CuO (001) facet-dependent. *Chem. Eng. J.* **2019**, *356*, 178–189. [\[CrossRef\]](#)
27. Kiani, R.; Mirzaei, F.; Ghanbari, F.; Feizi, R.; Mehdipour, F. Real textile wastewater treatment by a sulfate radicals-Advanced Oxidation Process: Peroxydisulfate decomposition using copper oxide (CuO) supported onto activated carbon. *J. Water Process Eng.* **2020**, *38*, 101623. [\[CrossRef\]](#)
28. Li, Z.; Liu, D.; Huang, W.; Wei, X.; Huang, W. Biochar supported CuO composites used as an efficient peroxymonosulfate activator for highly saline organic wastewater treatment. *Sci. Total Environ.* **2020**, *721*, 137764. [\[CrossRef\]](#)
29. Yin, Z.; Han, M.; Hu, Z.; Feng, L.; Liu, Y.; Du, Z.; Zhang, L. Peroxymonosulfate enhancing visible light photocatalytic degradation of bezafibrate by Pd/g-C₃N₄ catalysts: The role of sulfate radicals and hydroxyl radicals. *Chem. Eng. J.* **2020**, *390*, 124532. [\[CrossRef\]](#)

30. Xu, M.; Han, L.; Dong, S. Facile Fabrication of Highly Efficient g-C₃N₄/Ag₂O Heterostructured Photocatalysts with Enhanced Visible-Light Photocatalytic Activity. *ACS Appl. Mater. Interfaces* **2013**, *5*, 12533–12540. [[CrossRef](#)]
31. Kim, M.; Hwang, S.; Yu, J.S. Novel ordered nanoporous graphitic C₃N₄ as a support for Pt-Ru anode catalyst in direct methanol fuel cell. *J. Mater. Chem.* **2007**, *17*, 1656–1659. [[CrossRef](#)]
32. Liu, S.; Wei, X.; Lin, S.; Guo, M. Preparation of aerogel Mg(OH)₂ nanosheets by a combined sol-gel-hydrothermal process and its calcined MgO towards enhanced degradation of paraoxon pollutants. *J. Sol-Gel Sci. Technol.* **2021**, *99*, 122–131. [[CrossRef](#)]
33. Ali, J.; Jiang, W.; Shahzad, A.; Ifthikar, J.; Yang, X.; Wu, B.; Oyekunle, D.T.; Jia, W.; Chen, Z.; Zheng, L.; et al. Isolated copper ions and surface hydroxyl groups as a function of non-redox metals to modulate the reactivity and persulfate activation mechanism of spinel oxides. *Chem. Eng. J.* **2021**, *425*, 130679. [[CrossRef](#)]
34. Chen, C.; Liu, L.; Li, Y.; Li, W.; Zhou, L.; Lan, Y.; LI, Y. Insight into heterogeneous catalytic degradation of sulfamethazine by peroxymonosulfate activated with CuCo₂O₄ derived from bimetallic oxalate. *Chem. Eng. J.* **2020**, *384*, 123257. [[CrossRef](#)]
35. Guo, H.; Wang, Y.; Yao, X.; Zhang, Y.; Wang, Y. A comprehensive insight into plasma-catalytic removal of antibiotic oxytetracycline based on graphene-TiO₂-Fe₃O₄ nanocomposites. *Chem. Eng. J.* **2021**, *425*, 130614. [[CrossRef](#)]
36. Yousefi, A.; Alireza, N. Photodegradation pathways of phenazopyridine by the CdS-WO₃ hybrid system and its capability for the hydrogen generation. *Mater. Res. Bull.* **2022**, *148*, 111669. [[CrossRef](#)]
37. Guan, C.; Jiang, J.; Pang, S.; Chen, X.; Webster, R.D.; Lim, T.-T. Facile synthesis of pure g-C₃N₄ materials for peroxymonosulfate activation to degrade bisphenol A: Effects of precursors and annealing ambience on catalytic oxidation. *Chem. Eng. J.* **2020**, *387*, 123726. [[CrossRef](#)]
38. Song, H.; Liu, Z.; Guan, Z.; Yang, F.; Xia, D.; Li, D. Efficient persulfate non-radical activation of electron-rich copper active sites induced by oxygen on graphitic carbon nitride. *Sci. Total Environ.* **2021**, *762*, 143127. [[CrossRef](#)]
39. Zhang, S.; Gao, H.; Xu, X.; Cao, R.; Yang, H.; Xu, X.; Li, J. MOF-derived CoN/N-C@SiO₂ yolk-shell nanoreactor with dual active sites for highly efficient catalytic advanced oxidation processes. *Chem. Eng. J.* **2020**, *381*, 122670. [[CrossRef](#)]
40. Dan, J.; Rao, P.; Wang, Q.; Dong, L.; Chu, W.; Zhang, M.; He, Z.; Gao, N.; Deng, J.; Chen, J. MgO-supported CuO with encapsulated structure for enhanced peroxymonosulfate activation to remove thiamphenicol. *Sep. Purif. Technol.* **2022**, *280*, 119782. [[CrossRef](#)]
41. Qui Thanh Hoai, T.; Namgung, G.; Noh, J.-S. Facile synthesis of porous metal-doped ZnO/g-C₃N₄ composites for highly efficient photocatalysts. *J. Photochem. Photobiol. A Chem.* **2019**, *368*, 110–119.
42. Kang, Y.; Yang, Y.; Yin, L.-C.; Kang, X.; Liu, G.; Cheng, H.M. An Amorphous Carbon Nitride Photocatalyst with Greatly Extended Visible-Light-Responsive Range for Photocatalytic Hydrogen Generation. *Adv. Mater.* **2015**, *27*, 4572–4577. [[CrossRef](#)]
43. Liang, Q.; Li, Z.; Huang, Z.-H.; Kang, F.; Yang, Q.H. Holey Graphitic Carbon Nitride Nanosheets with Carbon Vacancies for Highly Improved Photocatalytic Hydrogen Production. *Adv. Funct. Mater.* **2015**, *25*, 6885–6892. [[CrossRef](#)]
44. Lee, S.J.; Begildayeva, T.; Jung, H.J.; Koutavarapu, R.; Yu, Y.; Choi, M.; Choi, M.Y. Plasmonic ZnO/Au/g-C₃N₄ nanocomposites as solar light active photocatalysts for degradation of organic contaminants in wastewater. *Chemosphere* **2021**, *263*, 128262. [[CrossRef](#)]
45. Song, H.; Guan, Z.; Xia, D.; Xu, H.; Yang, F.; Li, D.; Li, X. Copper-oxygen synergistic electronic reconstruction on g-C₃N₄ for efficient non-radical catalysis for peroxydisulfate and peroxymonosulfate. *Sep. Purif. Technol.* **2021**, *257*, 117957. [[CrossRef](#)]
46. Gao, Y.; Zhu, Y.; Lyu, L.; Zeng, Q.; Xing, X.; Hu, C. Electronic Structure Modulation of Graphitic Carbon Nitride by Oxygen Doping for Enhanced Catalytic Degradation of Organic Pollutants through Peroxymonosulfate Activation. *Environ. Sci. Technol.* **2018**, *52*, 14371–14380. [[CrossRef](#)]
47. Tsoncheva, T.; Ivanova, L.; Rosenholm, J.; Linden, M. Cobalt oxide species supported on SBA-15, KIT-5 and KIT-6 mesoporous silicas for ethyl acetate total oxidation. *Appl. Catal. B Environ.* **2009**, *89*, 365–374. [[CrossRef](#)]
48. Wu, M.; Li, L.; Xue, Y.; Xu, G.; Tang, L.; Liu, N.; Huang, W.-Y. Fabrication of ternary GO/g-C₃N₄/MoS₂ flower-like heterojunctions with enhanced photocatalytic activity for water remediation. *Appl. Catal. B Environ.* **2018**, *228*, 103–112. [[CrossRef](#)]
49. Harish, S.; Archana, J.; Sabarinathan, M.; Navaneethan, M.; Nisha, K.D.; Ponnusamy, S.; Muthamizhchelvan, C.; Ikeda, H.; Aswal, D.K.; Hayakawa, Y. Controlled structural and compositional characteristic of visible light active ZnO/CuO photocatalyst for the degradation of organic pollutant. *Appl. Surf. Sci.* **2017**, *418*, 103–112. [[CrossRef](#)]
50. Li, D.; Zan, J.; Wu, L.; Zuo, S.; Xia, D. Heterojunction tuning and catalytic efficiency of g-C₃N₄-Cu₂O with glutamate. *Ind. Eng. Chem. Res.* **2019**, *58*, 4000–4009. [[CrossRef](#)]
51. Zhang, J.; Zhang, M.; Zhang, G.; Wang, X. Synthesis of Carbon Nitride Semiconductors in Sulfur Flux for Water Photoredox Catalysis. *ACS Catal.* **2012**, *2*, 940–948. [[CrossRef](#)]
52. Parvari, R.; Ghorbani-Shahna, F.; Bahrami, A.; Azizian, S.; Assari, M.J.; Farhadian, M. A novel core-shell structured alpha-Fe₂O₃/Cu/g-C₃N₄ nanocomposite for continuous photocatalytic removal of air ethylbenzene under visible light irradiation. *J. Photochem. Photobiol. A Chem.* **2020**, *399*, 112643. [[CrossRef](#)]
53. Tian, Y.; Li, Q.; Zhang, M.; Nie, Y.; Tian, X.; Yang, C.; Li, Y. pH-dependent oxidation mechanisms over FeCu doped g-C₃N₄ for ofloxacin degradation via the efficient peroxymonosulfate activation. *J. Clean. Prod.* **2021**, *315*, 128207. [[CrossRef](#)]
54. Zhang, W.; Zhou, L.; Deng, H. Ag modified g-C₃N₄ composites with enhanced visible-light photocatalytic activity for diclofenac degradation. *J. Mol. Catal. A Chem.* **2016**, *423*, 270–276. [[CrossRef](#)]
55. Zhu, J.N.; Zhu, X.Q.; Cheng, F.F.; Li, P.; Xiong, W.W. Preparing copper doped carbon nitride from melamine templated crystalline copper chloride for Fenton-like catalysis. *Appl. Catal. B Environ.* **2019**, *256*, 117830. [[CrossRef](#)]
56. Li, H.; Guo, J.; Yang, L.; Lan, Y. Degradation of methyl orange by sodium persulfate activated with zero-valent zinc. *Sep. Purif. Technol.* **2014**, *132*, 168–173. [[CrossRef](#)]

57. Lu, H.; Sui, M.; Yuan, B.; Wang, J.; Lv, Y. Efficient degradation of nitrobenzene by Cu-Co-Fe-LDH catalyzed peroxymonosulfate to produce hydroxyl radicals. *Chem. Eng. J.* **2019**, *357*, 140–149. [[CrossRef](#)]
58. Timmins, G.S.; Liu, K.J.; Bechara, E.J.H.; Kotake, Y.; Swartz, H.M. Trapping of free radicals with direct in vivo EPR detection: A comparison of 5,5-dimethyl-1-pyrroline-N-oxide and 5-diethoxyphosphoryl-5-methyl-1-pyrroline-N-oxide as spin traps for HO and SO₄. *Free Radic. Biol. Med.* **1999**, *27*, 329–333. [[CrossRef](#)]
59. Zhang, J.; Zhao, W.; Wu, S.; Yin, R.; Zhu, M. Surface dual redox cycles of Mn(III)/Mn(IV) and Cu(I)/Cu(II) for heterogeneous peroxymonosulfate activation to degrade diclofenac: Performance, mechanism and toxicity assessment. *J. Hazard. Mater.* **2021**, *410*, 124623. [[CrossRef](#)]
60. Wang, Y.; Ji, H.; Liu, W.; Xue, T.; Liu, C.; Zhang, Y.; Liu, L.; Wang, Q.; Qi, F.; Xu, B.; et al. Novel CuCo₂O₄ Composite Spinel with a Meso-Macroporous Nanosheet Structure for Sulfate Radical Formation and Benzophenone-4 Degradation: Interface Reaction, Degradation Pathway, and DFT Calculation. *ACS Appl. Mater. Interfaces* **2020**, *12*, 20522–20535. [[CrossRef](#)]
61. Wang, R.; An, H.; Zhang, H.; Zhang, X.; Feng, J.; Wei, T.; Ren, Y. High active radicals induced from peroxymonosulfate by mixed crystal types of CuFeO₂ as catalysts in the water. *Appl. Surf. Sci.* **2019**, *484*, 1118–1127. [[CrossRef](#)]
62. Chen, C.; Liu, L.; Guo, J.; Zhou, L.; Lan, Y. Sulfur-doped copper-cobalt bimetallic oxides with abundant Cu(I): A novel peroxymonosulfate activator for chloramphenicol degradation. *Chem. Eng. J.* **2019**, *361*, 1304–1316. [[CrossRef](#)]
63. Li, Y.; Li, J.; Pan, Y.; Xiong, Z.; Yao, G.; Xie, R.; Lai, B. Peroxymonosulfate activation on FeCo₂S₄ modified g-C₃N₄ (FeCo₂S₄-CN): Mechanism of singlet oxygen evolution for nonradical efficient degradation of sulfamethoxazole. *Chem. Eng. J.* **2020**, *384*, 123361. [[CrossRef](#)]
64. Wu, S.; Liang, G.; Guan, X.; Qian, G.; He, Z. Precise control of iron activating persulfate by current generation in an electrochemical membrane reactor. *Environ. Int.* **2019**, *131*, 105024. [[CrossRef](#)]
65. Li, W.; Wang, Z.; Liao, H.; Liu, X.; Zhou, L.; Lan, Y.; Zhang, J. Enhanced degradation of 2,4,6-trichlorophenol by activated peroxymonosulfate with sulfur doped copper manganese bimetallic oxides. *Chem. Eng. J.* **2021**, *417*, 128121. [[CrossRef](#)]
66. Chen, K.; Zhang, X.-M.; Yang, X.-F.; Jiao, M.-G.; Zhou, Z.; Zhang, M.-H.; Wang, D.-H.; Bu, X.-H. Electronic structure of heterojunction MoO₂/g-C₃N₄ catalyst for oxidative desulfurization. *Appl. Catal. B Environ.* **2018**, *238*, 263–273. [[CrossRef](#)]
67. Li, H.; Yang, Z.; Lu, S.; Su, L.; Wang, C.; Huang, J.; Zhou, J.; Tang, J.; Huang, M. Nano-porous bimetallic CuCo-MOF-74 with coordinatively unsaturated metal sites for peroxymonosulfate activation to eliminate organic pollutants: Performance and mechanism. *Chemosphere* **2021**, *273*, 129643. [[CrossRef](#)]
68. Wagner, G.W.; Yang, Y.C. Rapid nucleophilic/oxidative decontamination of chemical warfare agents. *Ind. Eng. Chem. Res.* **2002**, *41*, 1925–1928. [[CrossRef](#)]
69. Ding, D.; Yang, S.; Chen, L.; Cai, T. Degradation of norfloxacin by CoFe alloy nanoparticles encapsulated in nitrogen doped graphitic carbon (CoFe@N-GC) activated peroxymonosulfate. *Chem. Eng. J.* **2020**, *392*, 123725. [[CrossRef](#)]
70. Oh, W.-D.; Chang, V.W.C.; Hu, Z.-T.; Goei, R.; Lim, T.-T. Enhancing the catalytic activity of g-C₃N₄ through Me doping (Me=Cu, Co and Fe) for selective sulfathiazole degradation via redox-based advanced oxidation process. *Chem. Eng. J.* **2017**, *323*, 260–269. [[CrossRef](#)]
71. Anipsitakis, G.P.; Dionysiou, D.D. Degradation of organic contaminants in water with sulfate radicals generated by the conjunction of peroxymonosulfate with cobalt. *Environ. Sci. Technol.* **2003**, *37*, 4790–4797. [[CrossRef](#)] [[PubMed](#)]
72. Shao, P.; Tian, J.; Yang, F.; Duan, X.; Gao, S.; Shi, W.; Luo, X.; Cui, F.; Luo, S.; Wang, S. Identification and Regulation of Active Sites on Nanodiamonds: Establishing a Highly Efficient Catalytic System for Oxidation of Organic Contaminants. *Adv. Funct. Mater.* **2018**, *28*, 1705295. [[CrossRef](#)]
73. Rasalingam, S.; Peng, R.; Koodali, R.T. An insight into the adsorption and photocatalytic degradation of rhodamine B in periodic mesoporous materials. *Appl. Catal. B Environ.* **2015**, *174*, 49–59. [[CrossRef](#)]
74. Natarajan, T.S.; Thomas, M.; Natarajan, K.; Bajaj, H.C.; Tayade, R.J. Study on UV-LED/TiO₂ process for degradation of Rhodamine B dye. *Chem. Eng. J.* **2011**, *169*, 126–134. [[CrossRef](#)]
75. Zhou, P.; Li, W.; Zhang, J.; Zhang, G.; Cheng, X.; Liu, Y.; Huo, X.; Zhang, Y. Removal of Rhodamine B during the corrosion of zero valent tungsten via a tungsten species-catalyzed Fenton-like system. *J. Taiwan Inst. Chem. Eng.* **2019**, *100*, 202–209. [[CrossRef](#)]
76. Vigneshwaran, S.; Karthikeyan, P.; Park, C.M.; Meenakshi, S. Boosted insights of novel accordion-like (2D/2D) hybrid photocatalyst for the removal of cationic dyes: Mechanistic and degradation pathways. *J. Environ. Manag.* **2020**, *273*, 111125. [[CrossRef](#)]
77. Chen, X.; Zhou, J.; Yang, H.; Wang, H.; Li, H.; Wu, S.; Yang, W. PMS activation by magnetic cobalt-N-doped carbon composite for ultra-efficient degradation of refractory organic pollutant: Mechanisms and identification of intermediates. *Chemosphere* **2022**, *287*, 132074. [[CrossRef](#)]
78. Pang, Y.; Kong, L.; Chen, D.; Yuvaraja, G.; Mehmood, S. Facilely synthesized cobalt doped hydroxyapatite as hydroxyl promoted peroxymonosulfate activator for degradation of Rhodamine B. *J. Hazard. Mater.* **2020**, *384*, 121447. [[CrossRef](#)]
79. Govarthanam, M.; Mythili, R.; Kim, W.; Alfarraj, S.; Alharbi, S.A. Facile fabrication of (2D/2D) MoS₂@MIL-88(Fe) interface-driven catalyst for efficient degradation of organic pollutants under visible light irradiation. *J. Hazard. Mater.* **2021**, *414*, 125522. [[CrossRef](#)]
80. Li, W.; Li, Y.; Zhang, D.; Lan, Y.; Guo, J. Enhanced kinetic performance of peroxymonosulfate/ZVI system with the addition of copper ions: Reactivity, mechanism, and degradation pathways. *J. Hazard. Mater.* **2020**, *393*, 121209. [[CrossRef](#)]

81. Chen, S.; Ma, L.; Du, Y.; Zhan, W.; Zhang, T.C.; Du, D. Highly efficient degradation of rhodamine B by carbon nanotubes-activated persulfate. *Sep. Purif. Technol.* **2021**, *256*, 117788. [[CrossRef](#)]
82. Xu, Y.; Hu, E.; Xu, D.; Guo, Q. Activation of peroxymonosulfate by bimetallic CoMn oxides loaded on coal fly ash-derived SBA-15 for efficient degradation of Rhodamine B. *Sep. Purif. Technol.* **2021**, *274*, 119081. [[CrossRef](#)]
83. Hu, L.; Deng, G.; Lu, W.; Lu, Y.; Zhang, Y. Peroxymonosulfate activation by Mn₃O₄/metal-organic framework for degradation of refractory aqueous organic pollutant rhodamine B. *Chin. J. Catal.* **2017**, *38*, 1360–1372. [[CrossRef](#)]
84. Liang, L.; Cheng, L.; Zhang, Y.; Wang, Q.; Meng, X. Efficiency and mechanisms of rhodamine B degradation in Fenton-like systems based on zero-valent iron. *RSC Adv.* **2020**, *10*, 28509–28515. [[CrossRef](#)]
85. Kong, L.; Fang, G.; Chen, Y.; Xie, M.; Zhu, F.; Ma, L.; Zhou, D.; Zhan, J. Efficient activation of persulfate decomposition by Cu₂FeSnS₄ nanomaterial for bisphenol A degradation: Kinetics, performance and mechanism studies. *Appl. Catal. B Environ.* **2019**, *253*, 278–285. [[CrossRef](#)]